INTERNATIONAL JOURNAL FOR NUMERICAL METHODS IN FLUIDS
Int. J. Numer. Meth. Fluids **31**: 535–577 (1999)

THE INFLUENCE OF TOPOGRAPHIC FEATURES AND DENSITY VARIATIONS UPON THE INTERNAL TIDES IN SHELF EDGE REGIONS

JIUXING XING AND ALAN M. DAVIES*

Proudman Oceanographic Laboratory, Bidston Observatory, Birkenhead, Merseyside L43 7RA, UK

SUMMARY

A brief outline of the development of a three-dimensional primitive equation baroclinic model for computing the internal tides is presented. A series of calculations are performed to examine the internal tide in the shelf edge region off the west coast of Scotland, with the aim of determining the influence upon the internal tide in the region of topographic features, namely large-scale features, such as seamounts, and small-scale features, such as a detailed specification of the shelf slope, which is possible using results from a recent survey rather than topographic data taken from a coarse grid model using depths interpolated from charts. The influence upon the solution of small variations in the density field and seasonal variations is examined. Also, the influence of a well-mixed bottom boundary layer at the base of the shelf slope, produced possibly by cascading of dense water off the shelf during a major wind event, upon the internal tide is also examined. In the calculations described here the model is used in cross-shelf form. A comparison of internal tides computed with and without the inclusion of an offshore seamount shows that internal tides are produced along the sides of the seamount, and can propagate towards the shelf edge, and thereby influence the internal tidal signal in that region. A comparison of internal tides computed using previously available bottom topography extracted from charts with those computed using a detailed topographic data set from a recent survey shows the importance of accurate topography in the shelf edge region for internal tide calculations. Simulations show that the internal tide is influenced by variations in the density field, suggesting that an accurately measured density field is essential for internal tide determination. Calculations also show that if a well-mixed sea bed boundary layer occurs at the bottom of the shelf slope, the internal tide can be reflected by this feature giving rise to significant internal tides in the ocean at larger distances from the shelf edge than in the absence of this water mass. Copyright © 1999 John Wiley & Sons, Ltd.

KEY WORDS: internal tides; topography; shelf edge; numerical model; seamount; cascading

1. INTRODUCTION

Early work [1,2] on examining the mechanisms influencing internal tide generation in shelf edge regions was primarily based upon analytical solutions, and was therefore restricted in the spatial variations of topography and density field which could be examined. This work also excluded the effects of internal friction and mixing upon the internal tides. However, it clearly identified the importance of bottom slope and vertical stratification upon the position of internal tide generation, and the propagation of the internal tide away from the generation site.

* Correspondence to: Proudman Oceanographic Laboratory, Bidston Observatory, Birkenhead, Merseyside L43 7RA, UK.

CCC 0271–2091/99/190535–43$17.50

Received April 1997
Revised August 1998

In the case of a subcritical slope, the internal tide propagation was predominantly onto the shelf, whereas with a supercritical slope, the internal tide propagation was predominantly back into the ocean.

In the case of physically realistic shelf edges, the shelf slope is not constant but varies continuously. Also the density field has significant spatial variability, giving rise in many cases to a range of internal tide generation sites and both subcritical and supercritical conditions for internal tide generation. A detailed examination of these problems is not possible using analytical models, and a range of numerical modelling approaches, based primarily on cross-sectional shelf models using various techniques from finite differences in the vertical [3–6] to using a modal expansion [7,8] has been developed. Although these models could accommodate arbitrary variations of bottom topography and density fields they did not include detailed parameterizations for the diffusion of momentum and density.

Recently, a three-dimensional baroclinic primitive equation model using a range of closure methods to parameterize subgrid scale mixing [9–11] has been used in a cross-shelf form to examine the influence of non-linear effects, and the parameterization of subgrid scale mixing on the generation of the internal tide in shelf edge regions. Although the effects of differences in density between winter and summer [12] upon the internal tides off the west coast of Scotland were examined using the model, no detailed investigation of the effect of rapid changes is density stratification, such as those above a well-mixed ocean bed layer at the bottom of the shelf slope, formed by cold water cascading down a slope, upon the internal tide were considered. Also no effects of significant changes in sea bed topography, such as those associated with sea mounts upon the internal tide, were examined, although there are significant spatial variations in the topography off the west coast of Scotland (Figure 1(a)). With detailed bottom topography now available from an extensive shelf edge survey [13] it is also possible to examine the influence of detailed topography and small changes in gradient down the shelf slope upon the internal tide. Here, this paper studies the effect of changes in shelf slope gradient upon the horizontal spatial variability of the tide, and the importance of this in determining a measurement strategy. In particular, the effects upon the internal tide of improving the accuracy of sea bed topography using data from a detailed survey collected at 57°N off the west coast of Scotland compared with that used previously by interpolating depths from a course grid (Figure 1(b)) model (grid resolution of order 4 km) of the region, is investigated.

Although three-dimensional models of the barotopic tide [14] and wind-driven flow off the west coast of Scotland have been developed and used to investigate the spatial and temporal variability of tidal and wind-driven flows in this region, no three-dimensional baroclinic model of the internal tide in the region has been developed. In this paper, such a three-dimensional model is developed and used in a cross-sectional form to examine the effect of topographic variations, such as the Hebrides Terrace seamount, and the influence of changes in the density field at depth upon the internal tide. The calculations presented here show that seamounts can produce local internal tides along their slopes, which can then propagate both out into the ocean and towards the shelf edge, thereby modifying the internal tide distribution produced at the shelf edge, which has been examined previously [9,10]. Also, changes in the density field at depth, associated with a well-mixed bottom boundary layer produced possibly by cold water cascading down the shelf slope, can influence the propagation of the internal tide. Although the influence of topography and stratification is considered here using a cross-sectional model, these effects are particularly important upon the three-dimensional internal tides in the region, and hence the understanding of their influence that can be gained from a cross-sectional model is vital before proceeding to the full three-dimensional solution. Although a full

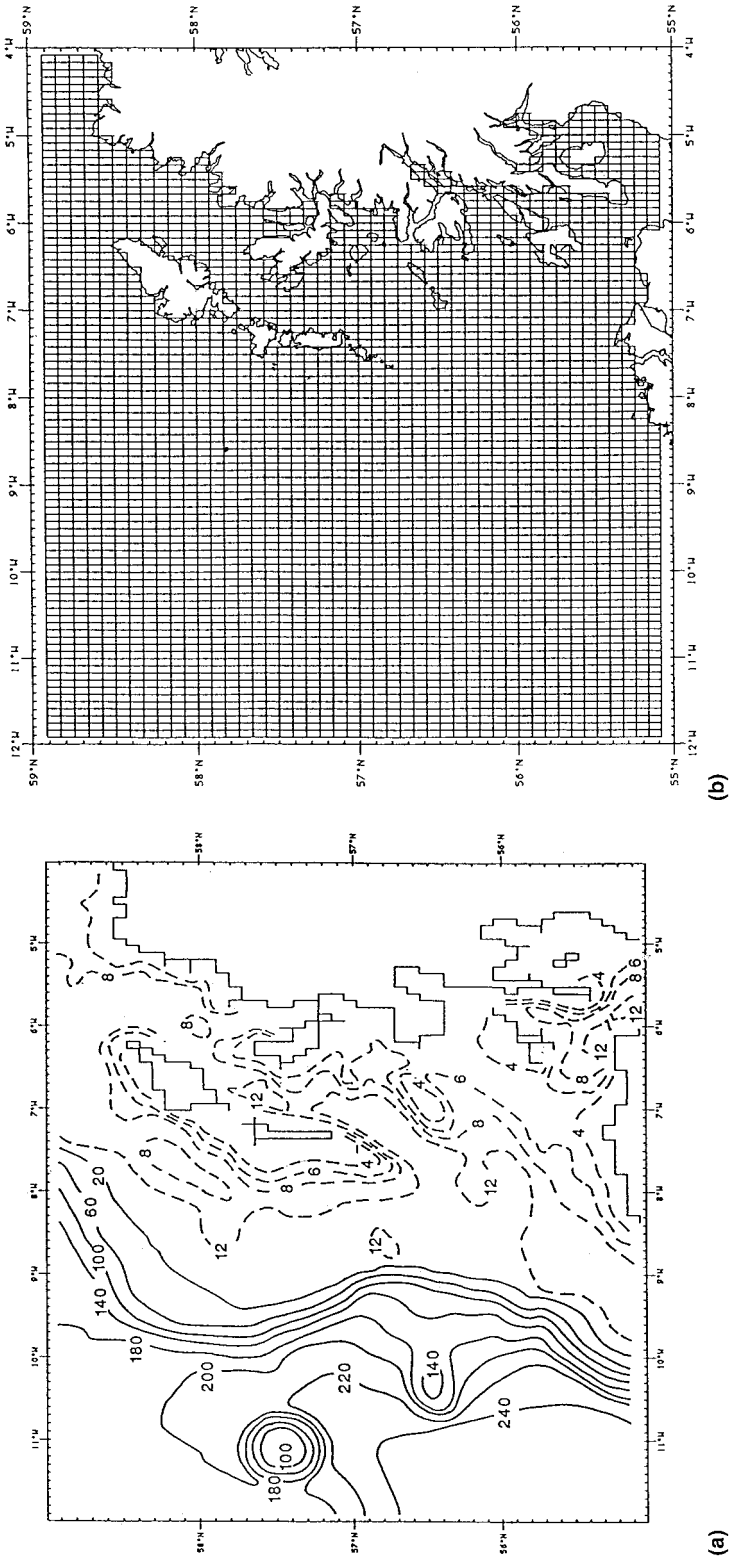

Figure 1. (a) Sea bed topography off the west coast of Scotland, contour intervals in decimetres, (b) finite difference grid of the three-dimensional west coast model, (c) (i) cross-shelf topography at 56.5°N and (ii) across-shelf component of the barotropic tidal current generated in the model.

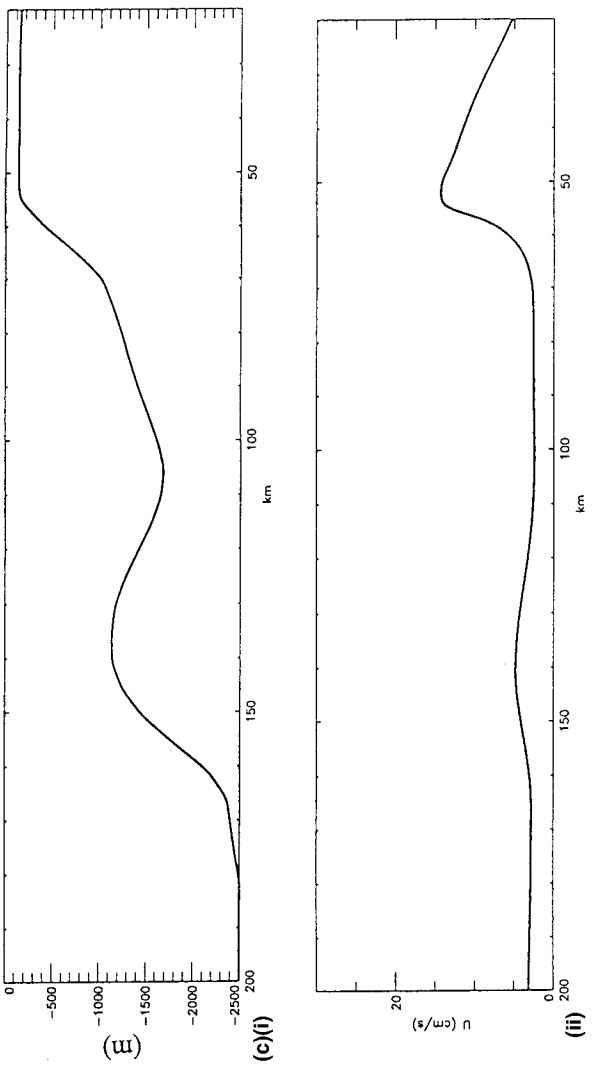

Figure 1 (*Continued*)

three-dimensional model is essential to describe the across-shelf and along-shelf propagation of the internal tide in a region such as the one considered here, where the across-shelf component of the internal tide dominates, then the use of a cross-section slice model is acceptable for the study considered here.

The mathematical development of the model and the numerical methods used to solve the hydrodynamic equations are given in the next section, with following sections describing the influence of topographic features, such as a seamount and abrupt changes in stratification at depth, upon the internal tide. Chances in topography from that used previously in a three-dimensional coarse grid model (Figure 1(a)) of the barotopic tide in the area [14] to that based upon a recent high resolution survey of the region [13] are also considered.

2. THE THREE-DIMENSIONAL INTERNAL TIDE MODEL

2.1. Primitive equations

Although the three-dimensional model is only used in cross-shelf form in the series of calculations presented subsequently, it is instructive to initially present the full three-dimensional equations, and then to state what are the consequences of approximating them to cross-sectional form. The three-dimensional baroclinic equations using the hydrostatic approximation, expressed in transport form using a sigma co-ordinate, $\sigma = (z - \zeta)/H$ in the vertical are given by

$$\frac{\partial Hu}{\partial t} + \nabla\cdot(Hu\vec{V}) + \frac{\partial Hu\omega}{\partial \sigma} - fHv = -gH\frac{\partial \zeta}{\partial x} + \mathrm{BPF}_x + \frac{1}{H^2}\frac{\partial}{\partial \sigma}\left(K_m\frac{\partial Hu}{\partial \sigma}\right) + HF_u, \tag{1}$$

$$\frac{\partial Hv}{\partial t} + \nabla\cdot(Hv\vec{V}) + \frac{\partial Hv\omega}{\partial \sigma} + fHu = -gH\frac{\partial \zeta}{\partial y} + \mathrm{BPF}_y + \frac{1}{H^2}\frac{\partial}{\partial \sigma}\left(K_m\frac{\partial HV}{\partial \sigma}\right) + HF_v, \tag{2}$$

$$\frac{\partial \zeta}{\partial t} + \nabla\cdot\left(\int_{-1}^{0}(H\vec{V})\,\mathrm{d}\sigma\right) = 0, \tag{3}$$

$$\frac{\partial HT}{\partial t} + \nabla\cdot(HT\vec{V}) + \frac{\partial HT\omega}{\partial \sigma} = \frac{1}{H^2}\frac{\partial}{\partial \sigma}\left(K_h\frac{\partial HT}{\partial \sigma}\right) + HF_T, \tag{4}$$

$$\frac{\partial P}{\partial \sigma} = -\rho gH. \tag{5}$$

In the calculations described subsequently, the density was computed from the temperature using an idealized equation of state given by

$$\rho = \rho_0(1 - \alpha(T - T_0)). \tag{6}$$

In these equations, $\vec{V} = (u, v)$ and (u, v, ω) are the velocity components corresponding to the (x, y, σ) co-ordinates, with x the cross-shelf co-ordinate, and y the along-shelf axis; ρ is the density; T is the temperature; α is the thermal expansion coefficient: T_0 and ρ_0 are the reference temperature and density respectively; H is the total water depth; ζ is the elevation of the sea surface above the undisturbed level; z is the water depth increasing vertically upwards with $z = \zeta$, the free-surface and $z = -h$, the sea bed; f is the Coriolis parameter, g is the gravitational acceleration; t is time; K_m, and K_h are vertical eddy viscosity and diffusivity coefficients; F_u, F_v and F_T are horizontal diffusions for the momentum and temperature; P is the pressure field. The exact form of the baroclinic pressure force terms (BPF_x, BPF_y) are given in [15] and will not be repeated here.

In the calculations described subsequently, the model was used in cross-shelf form. Consequently, terms involving along-shelf pressure gradients, and along-shelf variations of velocity were zero. However, the along-shelf velocity, the Coriolis term and the vertical viscous term in Equation (2) was non-zero. For internal tides the retention of the Coriolis term is important [1,2,8]. The consequences of using a two-dimensional cross-section model are that there is no along-shelf change in topography, also it is not possible to study the along-shelf variation of the tide. However, the influence of rotation and along-shelf flow is retained, which is sufficient for the study considered here.

The horizontal diffusion terms F_u, F_v and F_T in Equations (1), (2) and (4) are parameterized in terms of either a Laplacian or a biharmonic horizontal viscous term [16]. Calculations were performed with both the Laplacian and biharmonic forms of horizontal diffusion with diffusion coefficients of 10 $m^2 s^{-1}$ (Laplacian diffusion) and 10^6 $m^4 s^{-2}$ (biharmonic diffusion), with these low values and the fine finite difference grid used in the model, no significant differences were found in the solutions, and the biharmonic form was used in all calculations, to ensure minimum damping of the waves, that could be accurately resolved on the model grid. Identical horizontal diffusion coefficients for temperature, turbulence and momentum were used.

A time splitting method is used to integrate the hydrodynamic equations in order to reduce the computational time, with the velocity expressed as a depth mean velocity (external mode) and a depth dependent velocity (internal mode). Since the external mode represents the fast moving gravity waves, a small time step is required for the time integration of the free-surface wave that involves u and v in order to satisfy the CFL condition. The internal mode, however, represents slow moving waves and hence much larger time steps can be used (see [17–19] for details). In the calculations described subsequently, the external mode had a time step of 2.79 s in order to satisfy the CFL condition, although a longer time step upto a factor of 50 times longer could be used for the internal modes. A central differencing method was employed for the advection of momentum, although a total variation diminishing (TVD) scheme [20] was used for the advection of density and temperature [9]. The vertical diffusion terms that are computed using a two-equation turbulence energy model, are computed by a semi-implicit time integration method in order to avoid the use of a short time step when a fine grid is used in the vertical. Details of the method can be found in [18,19,21,22]. A staggered Arakawa C uniform finite difference grid is used in the horizontal with a variable grid in σ co-ordinates in the vertical.

The numerical solution of the hydrodynamic equations in cross-shelf form involves a finite difference grid of the order of 50 σ levels in the vertical, with enhanced resolution in the near-bed region, in order to resolve the increase in shear in this area. Calculations involving the comparison of numerical solutions [10] with analytical solutions of Craig [2], showed that an across-shelf grid resolution of 0.625 km was necessary in order to accurately represent the internal tidal solutions of Craig [2], and this resolution was used in the calculations reported here.

2.2. Turbulence energy model

Although a number of turbulence energy models exist in the literature [23–26], and simpler formulations in terms of a Richardson number-dependent viscosity [27], the determination of the vertical eddy viscosity and diffusivity is accomplished here using the well-established two-equation formulation given by Blumberg and Mellor [28]. This method involves prognostic equations for the turbulence energy and mixing length, and is commonly known as the

$q^2 - q^2\ell$ model, where $q^2 = 2E$, with E the turbulence kinetic energy (TKE) and ℓ the mixing length, and has been used in a number of shallow sea models (e.g. [29]).

The equations for this turbulence energy model in σ co-ordinates are given by

$$\frac{\partial q^2 H}{\partial t} + \nabla\cdot(Hq^2\vec{V}) + \frac{\partial Hq^2\omega}{\partial\sigma} = 2\frac{K_m}{H}\left[\left(\frac{\partial u}{\partial\sigma}\right)^2 + \left(\frac{\partial v}{\partial\sigma}\right)^2\right] + \frac{2gK_h}{\rho}\frac{\partial\rho}{\partial\sigma} - \frac{2q^3H}{B_1\ell} + \frac{1}{H^2}\frac{\partial}{\partial\sigma}\left(S_q q\ell\frac{\partial q^2 H}{\partial\sigma}\right) + HF_q \tag{7}$$

and

$$\frac{\partial q^2\ell H}{\partial t} + \nabla\cdot(Hq^2\vec{V}\ell) + \frac{\partial Hq^2\ell\omega}{\partial\sigma} = \frac{\ell E_1 K_m}{H}\left[\left(\frac{\partial u}{\partial\sigma}\right)^2 + \left(\frac{\partial v}{\partial\sigma}\right)^2\right] + \frac{\ell E_1 gK_h}{\rho}\frac{\partial\rho}{\partial\sigma} - \frac{q^3}{B_1}W + \frac{1}{H^2}\frac{\partial}{\partial\sigma}\left(S_q q\ell\frac{\partial q^2\ell}{\partial\sigma}\right) + HF_\ell, \tag{8}$$

with F_q and F_ℓ the horizontal diffusion of q^2 and $q^2\ell$ respectively.

The wall proximity function W is defined as in Blumberg and Mellor [28], with $\kappa = 0.4$ the Von Karman constant, and the other coefficients given by $S_q = 0.2$, $B_1 = 16.6$, $E_1 = 1.8$, $E_2 = 1.33$.

The diffusion coefficients for momentum K_m (namely eddy viscosity) and density K_h (namely eddy diffusivity) are computed from

$$K_m = \ell q S_M, \qquad K_h = \ell q S_H, \tag{9}$$

with the algebraic form of the stability functions S_M and S_H, identical to those used by Galperin *et al.* [30,31], and will not be presented here.

A limiting condition [31] is applied to ℓ of the form

$$\ell \le \frac{k_1 q}{N}, \tag{10}$$

with k_1 a specified constant [26] and N the buoyancy frequency.

2.3. Boundary conditions

At sea surface and sea bed there is no heat flux, and for tidally forced motion, the surface stress is zero. At the sea bed a quadratic bottom friction condition is applied with a drag coefficient corresponding to a bed roughness length $z_0 = 0.005$ m. At the sea surface there is no flux of turbulence energy and the length scale ℓ tends to a small value z_S, which is the sea surface roughness length. At the sea bed a balance of production, dissipation and diffusion is assumed [18], with the length scale the bed roughness length z_0.

At coastal boundaries, the normal component of current and the horizontal gradient of temperature and turbulence are taken as zero. A radiation-type open boundary condition e.g. [32] is applied at sea boundaries.

3. INTERNAL TIDE CALCULATIONS AT 56.6°N (THE INFLUENCE OF SEAMOUNTS)

In this series of calculations, the generation of the internal tide due to M_2 tidal forcing is considered using a cross-shelf model with topography corresponding to that at 56.5°N off the

west coast of Scotland (Figure 1(a)). The shelf slope in this region is characterized by an increase in water depths between 60 and 105 km offshore (Figure 1(c)) with a subsequent decrease in water depths in the region of the Hebrides Terrace Seamount (Figure 1(c)), with water depths increasing to oceanic to the west of this. This region is chosen because it is in the area (Figure 1(a)) of a planned oceanographic measurement exercise where cross-shelf measurements will be taken in areas with a range of topographic features (Figure 1(a)). It is, therefore, important to examine the influence of the seamount upon the internal tide in the region.

In all calculations described subsequently, the model was forced by the principal semidiurnal lunar barotropic tide [denoted as the M_2 tidal constituent [33], which has a period of 12.42 h] at its western open boundary. In all calculations the same amplitude and phase of this tidal forcing were used throughout. This forcing was chosen to produce typical observed M_2 tides in the region, namely across-shelf barotropic tidal currents at the top of the shelf break of order 20 cm s^{-1} (Figure 1(c)ii). The model was integrated forward in time with tidal forcing from an initial state in which an observed typical winter or summer temperature profile [12] was specified, for the order of 30 tidal cycles and results over the last M_2 tidal period were saved for harmonic analyse. By using harmonic analysis methods the amplitude and phase of the M_2 tide, and its first and second harmonics, namely M_4 (period 6.21 h) and M_6 (period 4.14 h) could be separated. Since the primary aim here is a process study to examine the influence upon the internal tide of a range of factors, namely topography (both large-scale, namely seamounts, and small-scale, namely variations in topography down the shelf slope) and stratification effects due to cascading, then it is acceptable to use typical temperature profiles and an idealized equation of state (Equation (6)). If the primary objective was a detailed simulation of the internal tides then a more complex equation of state and a detailed survey of the density field would be required. In this section, besides examining the influence of seamounts upon the generation of the internal tide, a number of calculations are performed with and without the non-linear terms in the hydrodynamic equations in order to examine the influence of these terms. It is important to determine the influence of the non-linear terms since a number of modelling studies in the literature have neglected these terms. Calculations are also performed with a slightly modified winter density profile in order to determine the influence upon the internal tide of small changes in the density field that might occur from sampling errors during an experiment or from spatial variability, which cannot be resolved by a limited number of measurements. Finally, in this section results are presented using a typical summer stratification to examine seasonal variability in a region of internal tide generation in the presence of seamounts.

3.1. Winter stratification with seamount and linear model

In an initial calculation with winter stratification (Figure 2) (Table I calculation 1) the non-linear advection of the momentum terms that produce the higher tidal harmonics [9] were omitted from the equations, giving in essence a linear model (naturally the advection of density was retained). A typical winter temperature profile was used as the initial state and the model was integrated forward in time for 30 tidal cycles and results from the last M_2 period were harmonically analysed to yield the distributions of across-shelf internal tidal current amplitudes (U) and internal displacements amplitudes, which are contoured in Figure 3(a) and (b). Since a mode splitting technique is used in the model it is advantageous to define the internal modal current as being due to the internal tide since current structure (i.e. the internal mode) is generated primarily by internal pressure gradients due to the internal tide. However, some

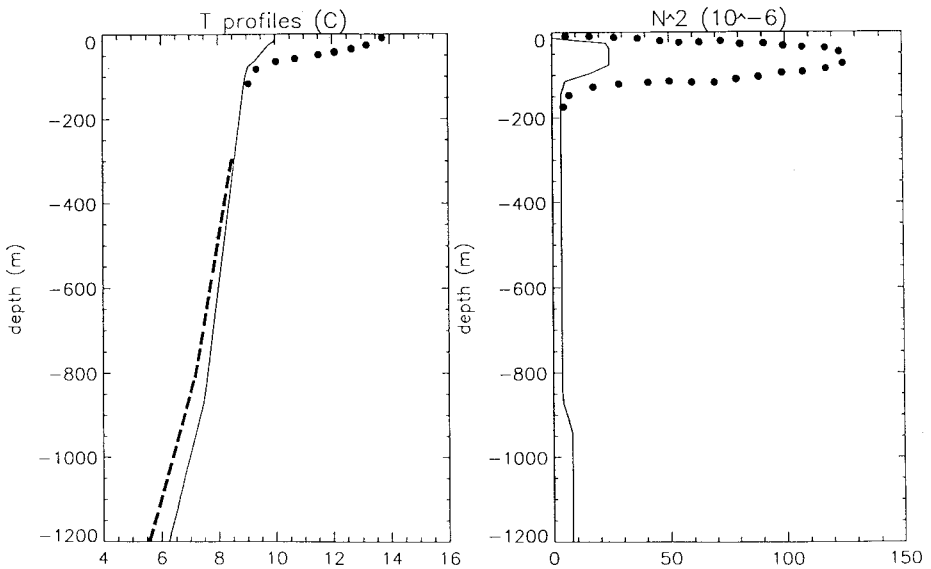

Figure 2. Vertical profile of temperature and buoyancy frequency (N^2), for winter (solid line) perturbed winter (dashed line) and summer (dotted line). [Note: the dashed line and solid line coincide above 300 m, similarly the dotted and solid line coincide below 100 m. Also to the scale shown here the buoyancy frequency (N^2) computed with the solid and dashed line cannot be distinguished from each other.]

current structure is generated by viscous effects that are included in this term. Thus, the instantaneous internal tidal current u' is computed using $u' = u - \bar{u}$, where $\bar{u}$ is the instantaneous depth mean current. The internal displacement amplitude (η) is computed from $\eta = W_a/\omega_t$, where W_a is the amplitude of the vertical velocity (in z co-ordinates) and ω_t is the tidal frequency. The internal displacement amplitude corresponds to the amplitude of the

Table I. A series of calculations (1–10) indicating different scenarios

Calculation	Momentum: linear (L); non-linear (NL)	Seamount	Stratification
Cross-section 56.5°N			
1	L	Yes	Winter
2	NL	Yes	Winter
3	NL	No	Winter
4	NL	Yes	Perturbed winter
5	NL	No	Perturbed winter
6	NL	Seamount only	Perturbed winter
7	L	Yes	Summer
8	NL	Yes	Summer
Calculation	**Stratification**	**Topography**	
Cross-section 57°N			
9	Winter	Original	
10	Modified winter	Original	
11	Winter	Accurate survey	

vertical variation of a density surface from its equilibrium position at a given frequency (in the present case the M_2, M_4 or M_6 frequency) due to the internal tide. It is important to note that during the period of the calculation besides the advection of density by the tidal current, the density field changes due to mixing produced by the tidal turbulence [9,10] and hence will no longer correspond exactly to the initial density field.

Contours of M_2 tidal current amplitude and displacement (Figure 3(a) and (b)) show a region of enhanced near-bed current and internal displacement at the top of the shelf slope (at about 60 km offshore) associated with the production of the internal tide in this region, with some internal tide propagating slightly onto the shelf. A second internal tide generation point occurs at depth below 1000 m approximately 70 km offshore and is associated with a change in gradient of the bottom slope, and gives rise to an intensification of bottom currents at this location. Regions of intensified surface current at approximately 50 and 80 km offshore associated with the propagation of the internal tide from these points along internal ray paths [4,5,7,8,34–36] are also shown in Figure 3(a), and are characteristic of the computation of the internal tide on a shelf slope [9]. Of particular interest in the present series of calculations is the intensification of the near bed u current amplitude and displacement on the western and eastern sides of the sea mount, and the region of intensified internal displacement above the

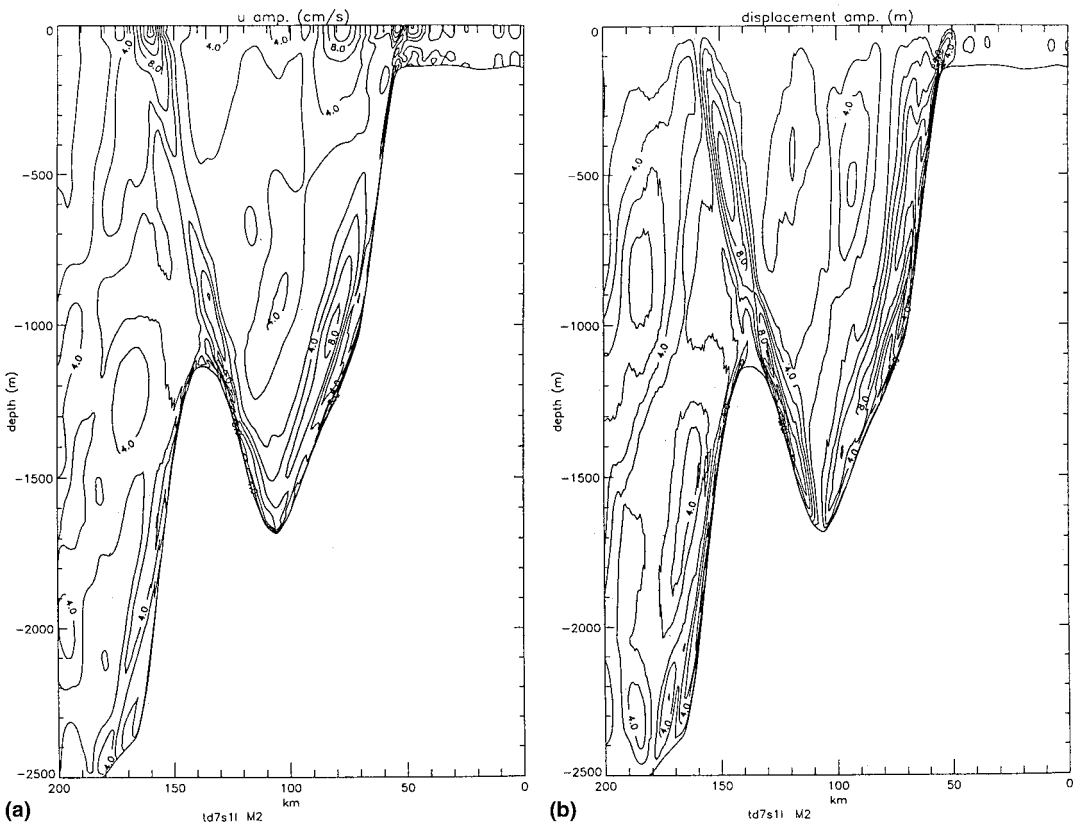

Figure 3. Contours of (a) the amplitude (cm s^{-1}) of the across-shelf (u component) of internal tidal current, (b) the internal displacement (m) at the M_2 frequency, and (c) viscosity ($\log_{10}$, $m^2\,s^{-1}$) averaged over an M_2 tidal cycle, and (d) instantaneous values of σ_t computed with the linear model and winter stratification.

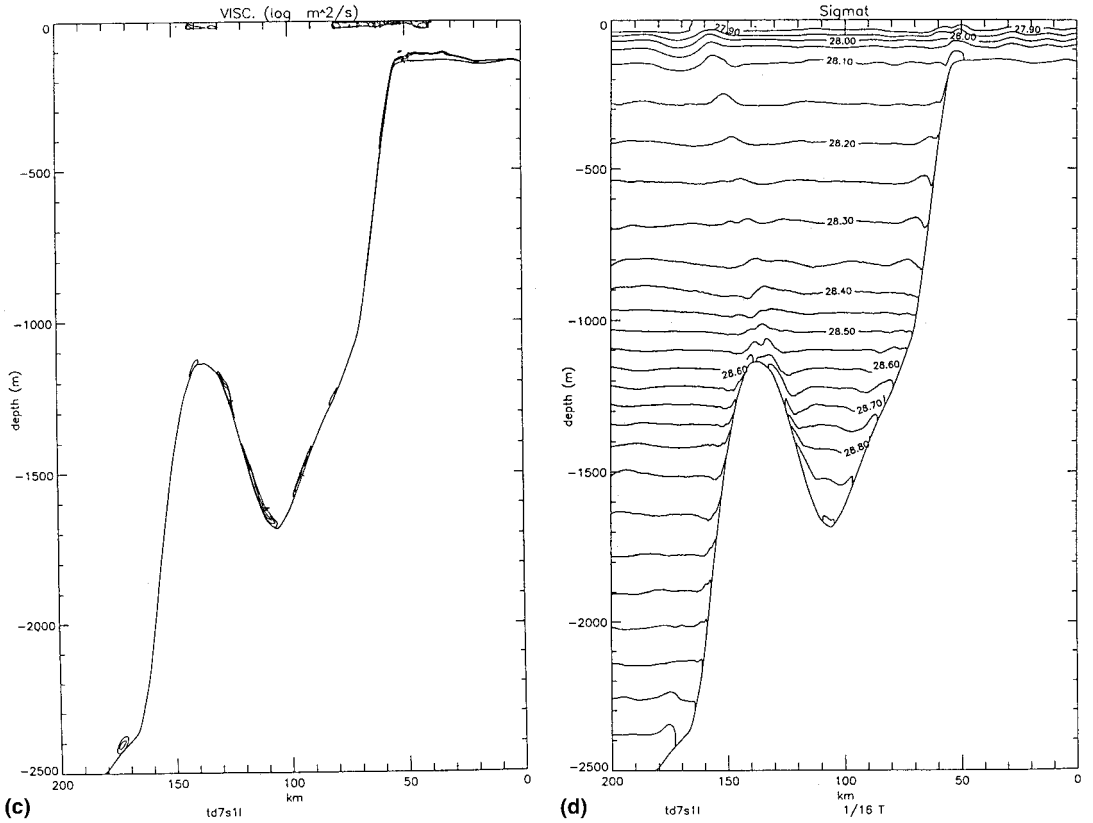

Figure 3 (*Continued*)

sea mount extending offshore to a distance of 160 km at the surface. The surface current amplitude is also intensified at this point, with an amplitude exceeding 12 cm s^{-1}.

Regions of intensified surface and bed turbulence energy (not shown) and eddy viscosity associated with these areas of enhanced current shear are clearly evident in Figure 3(c). Although only eddy viscosity is shown here, eddy diffusivity and turbulence energy show similar distributions.

Contours of the density surfaces (an instantaneous picture after 30 tidal cycles) show (Figure 3(d)) a region of increased bed mixing on the shelf and in the upper part of the shelf slope. (For clarity, contours of sigma-t (σ_t) defined by $\sigma_t = \rho(\mathrm{kg\,m^{-3}}) - 1000$, where ρ is the density of sea water, are plotted here rather than contours of density in kg m^{-3}). Upwelling of the density surfaces along the western and eastern sides of the seamount is clearly seen as is the evidence of short wavelength internal waves between the eastern side of the seamount and the continental slope, with enhanced mixing occurring in this region (Figure 3(c)). Above the seamount there is a significant displacement of the density surfaces extending from the sea bed to the point at the sea surface located 160 km offshore where the region of increased surface mixing occurs. The intensification of the displacement of the density surface at the sea bed to the east of the seamount, the reduction of this displacement at above 700 m and its significant enhancement around 500 m corresponds to the contours of internal displacements in this region shown in Figure 3(b).

Before considering in detail the effect of the seamount upon the internal tide, it is instructive to consider the solution with the inclusion of the non-linear terms that can generate the higher harmonics of the tide [9].

3.2. Winter stratification with seamount and non-linear terms

In a second calculation (Table I, calculation 2), the non-linear momentum terms that produce the higher tidal harmonics were retained. Identical initial conditions and duration of time integration to that described previously were used in the calculation, which was subsequently harmonically analysed in order to examine the M_2 and M_4 components of the internal tide.

Contours of the amplitude of the u component of the M_2 tide (Figure 4(a)) show regions of intensified bed current along the slope at approximately 60 km offshore, where the gradient of the shelf edge topography changes. The intensity of these bottom currents and magnitudes of the internal displacements (Figure 4(b)) in this region is larger than those found in the linear case (compare Figure 4(a) and (b) with Figure 3(a) and (b)).

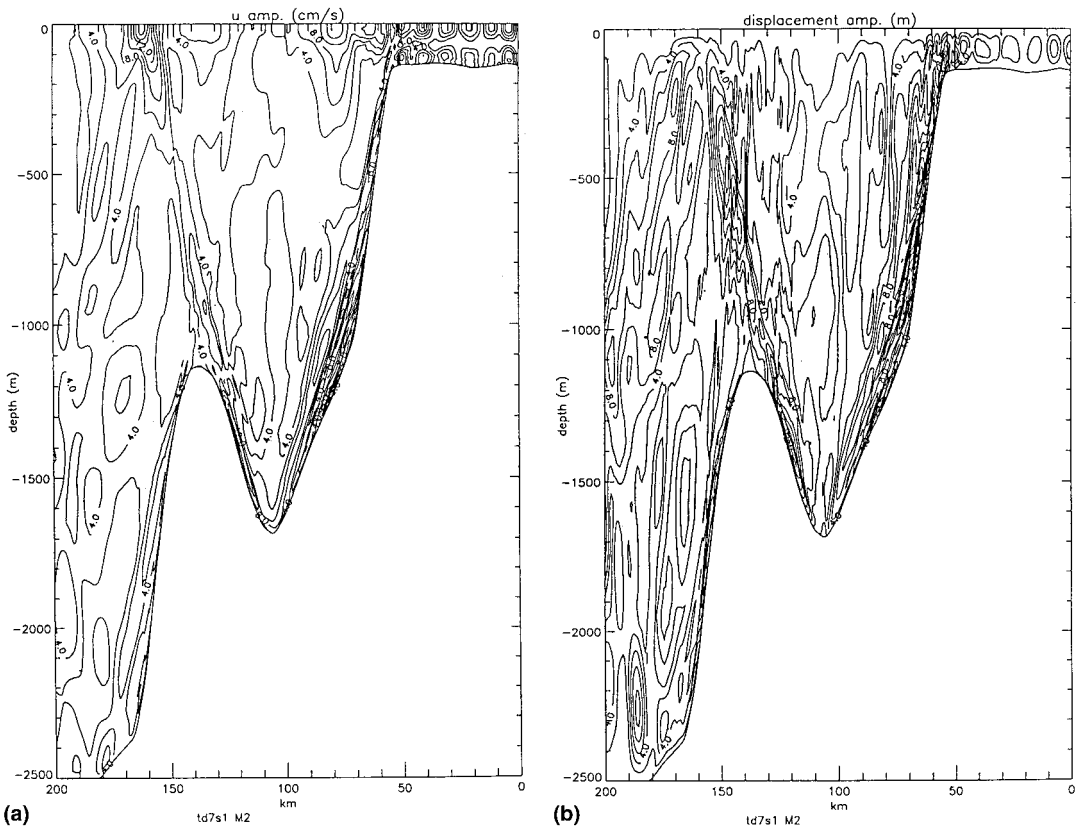

Figure 4. Contours of (a) the amplitude (cm s^{-1}) of the internal tidal current, (b) internal displacement (m) at the M_2 frequency, (c) (i) viscosity ($\log_{10}$ $m^2 s^{-1}$), mean over an M_2 tidal cycle, (ii) expanded plot at top of shelf, (d) instantaneous values of σ_t, (e) amplitude (cm s^{-1}) of the M_4 internal tidal currents and (f) internal displacement (m) of the M_4 tide, computed with the non-linear model and winter stratification.

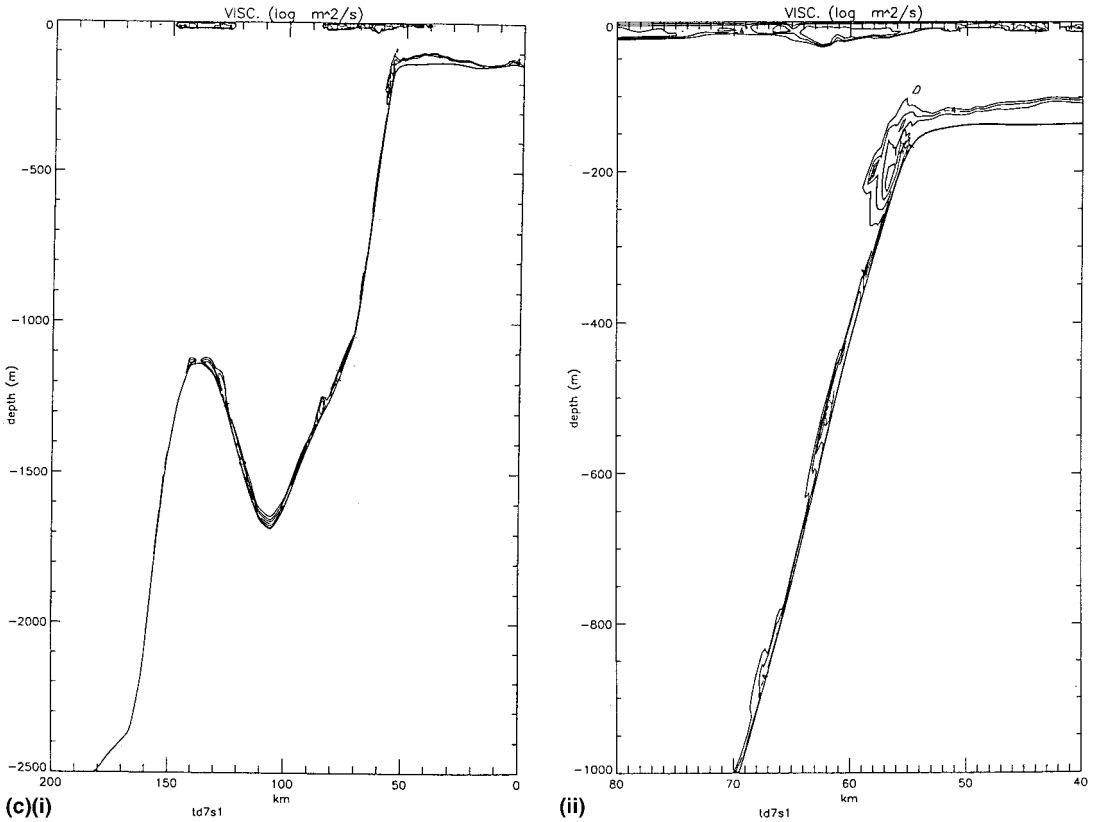

Figure 4 (*Continued*)

On the shelf there are regions of strong surface and bottom current separated in phase by 180°, (contours of phase lines not shown) suggesting the propagation of a mode two internal tide onto the shelf, which was not present in the previous calculation (compare Figure 4(a) with Figure 3(a)). This change in propagation of the internal tide suggests that the density field at the shelf break is different from that occurring in the linear model, due to differences in mixing intensity in the shelf break region. Xing and Davies [9] showed from a comparison of linear and non-linear internal tide calculations that when the non-linear terms are present short wavelength internal waves are generated at the shelf break and the horizontal mixing associated with these is much larger than in the linear model. Details of the density field will be considered later. Regions of intensified bottom currents and displacements are also evident on the western and eastern side of the seamount, with an area of enhanced internal displacement above the sea mount extending towards the surface at approximately 160 km offshore. This region is similar to that found with the linear model, (compare Figures 4(b) and 3(b)), although the spatial variability in the non-linear model is significantly greater than that in the linear model due to the production of short waves due to the non-linear terms [9].

Contours of current amplitude (Figure 4(a)) show a region of strong (exceeding 16 cm s^{-1}) surface current at approximately 160 km offshore. The current magnitude in this region is significantly larger than that found previously (compare Figures 4(a) and 3(a)). Although spatial contours of viscosity (Figure 4(c)) (note Figure 4(c)i is for the whole domain with

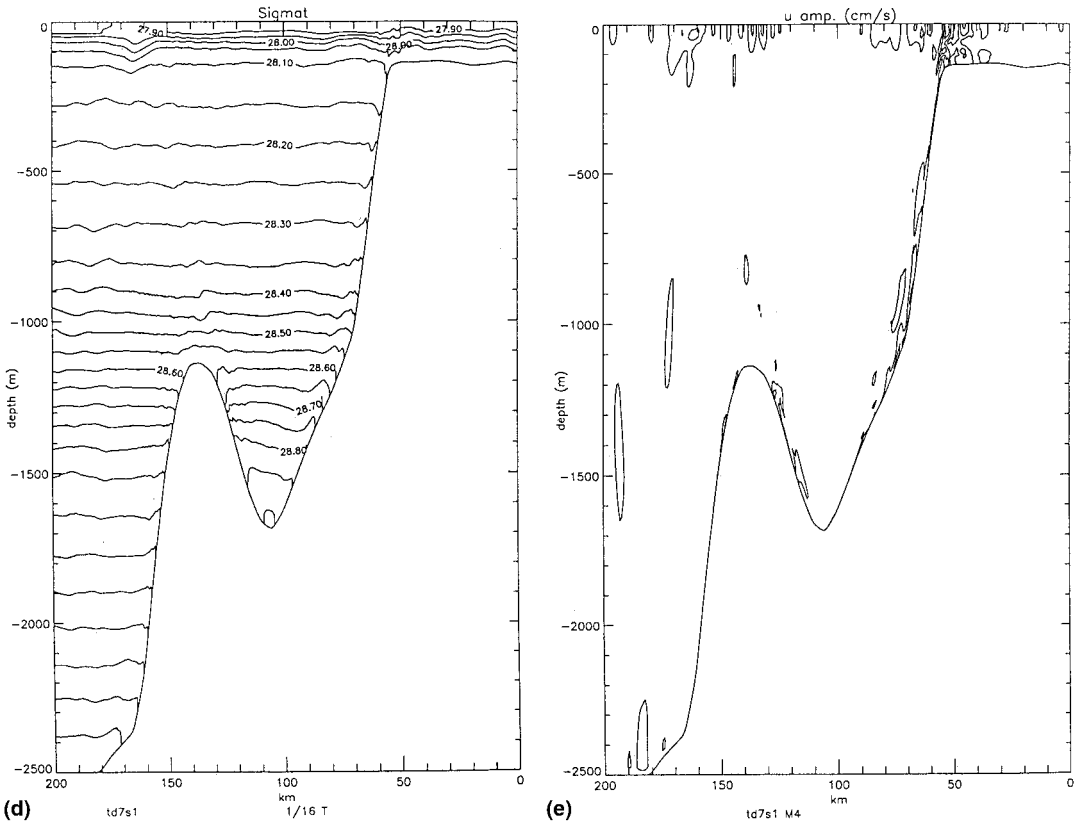

Figure 4 (*Continued*)

Figure 4(c)ii an expanded version of a more limited area to show detail at the top of the shelf) show similar distributions to those found in the linear case, it is evident that the magnitude is much larger, associated with the stronger shear due to the more intense currents.

In order to understand the differences between the linear and non-linear solutions, it is instructive to compare the computed density fields at the same moments in time (Figures 4(d) and 3(d)). From a comparison of Figures 4(d) and 3(d), it is evident that above the shelf break at about 55 km offshore there are a number of short waves on the density surfaces in the upper 100 m of the water column that were not present in the linear solution. Although in the present model short waves are smoothed by horizontal diffusion, they are still present in the non-linear calculation and hence can give rise to enhanced mixing. On the upper part of the shelf slope (above 700 m) from the bottom boundary layer, there is some evidence of downwelling, as compared with upwelling in the linear case (compare Figures 4(d) and 3(d)), suggesting a difference in phase of the internal tide in this region between the linear and non-linear solution due to local changes in the density field along the upper part of the shelf slope. Similar differences between upwelling (Figure 3(d)) and downwelling (Figure 4(d)) are evident on the eastern side of the seamount. Above the seamount there is evidence of enhanced displacement as in the linear model, particularly in the near surface density fields, although at depth the generation of short internal waves due to the non-linear terms gives a more complex spatial distribution than that found in the linear model.

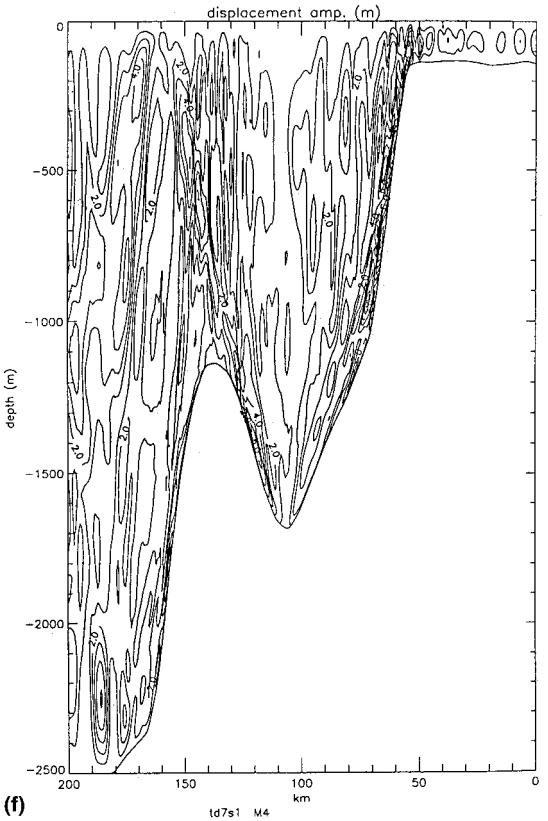

Figure 4 (*Continued*)

The spatial distribution (Figure 4(e) and (f)) of the M_4 current amplitude and displacement at depth shows an increase in magnitude above the shelf break, where the non-linear terms are important and along the shelf slope at depth and in the surface layer above the seamount.

This comparison of solutions with and without the non-linear terms in a region of seamounts clearly shows that it is important to retain the non-linear terms in any modelling work. The seamount clearly has an influence upon the internal tide although this can only be examined by using the model with the inclusion of the non-linear terms due to their influence upon the solution. In order to examine the role of the seamount in detail, the next section considers the calculation of the internal tide in the absence of the seamount.

3.3. Winter stratification in the absence of the seamount but including the non-linear terms.

In this calculation (Table I, calculation 3), the seamount was removed by linearly interpolating the bottom topography from 165 km offshore to 105 km, giving a smooth continuous increase in depth down the shelf slope. Although such a change to the water depth is artificial, the calculations without the seamount give some indication of the role of such a feature.

Comparing contours of u current amplitude (Figures 5(a) and 4(a)), it is evident that the mode-two internal tide on the shelf is not significantly affected by the presence of the seamount nor is the intensification of the near bed currents along the shelf slope at a depth of about 1000 m. However, currents and internal displacements at this depth at approximately

140 km offshore (a point previously above the seamount) show very significantly different distributions (Figure 5(a) and (b)) to those found previously (Figure 4(a) and (b)), in particular a much smoother spatial variation of current amplitude and displacement is evident, the reasons for which will be discussed subsequently. The intensification of the surface current at approximately 160 km offshore is still evident, although its magnitude has been reduced, suggesting that this is produced primarily by the internal tide generated along the shelf slope, with a contribution from the internal tide generated at the seamount.

From a comparison of contours of eddy viscosity (Figures 5(c) and 4(c)) [note contours are given for the whole region of Figures 5(c)i and 4(c)i with a more detailed plot at the top of the shelf slope in Figures 5(c)ii and 4(c)ii], it is evident that mixing at the top of the shelf break and in the surface layer above this is not affected by the seamount. However, along the shelf slope, particularly at a depth of 1500 m, there are some differences in the mixing associated with the removal of the seamount. Also, the seamount appears to have some influence upon the surface mixing at approximately 180 km offshore, which is reduced when the seamount is removed.

To understand the role of the seamount it is instructive to compare σ_t distributions without the seamount with those including the seamount at the same moment in time (Figures 5(d) and 4(d)). From this comparison it is evident that σ_t contours on the shelf and above the top of the shelf slope (Figure 5(d)) are not significantly different from those computed with the seamount

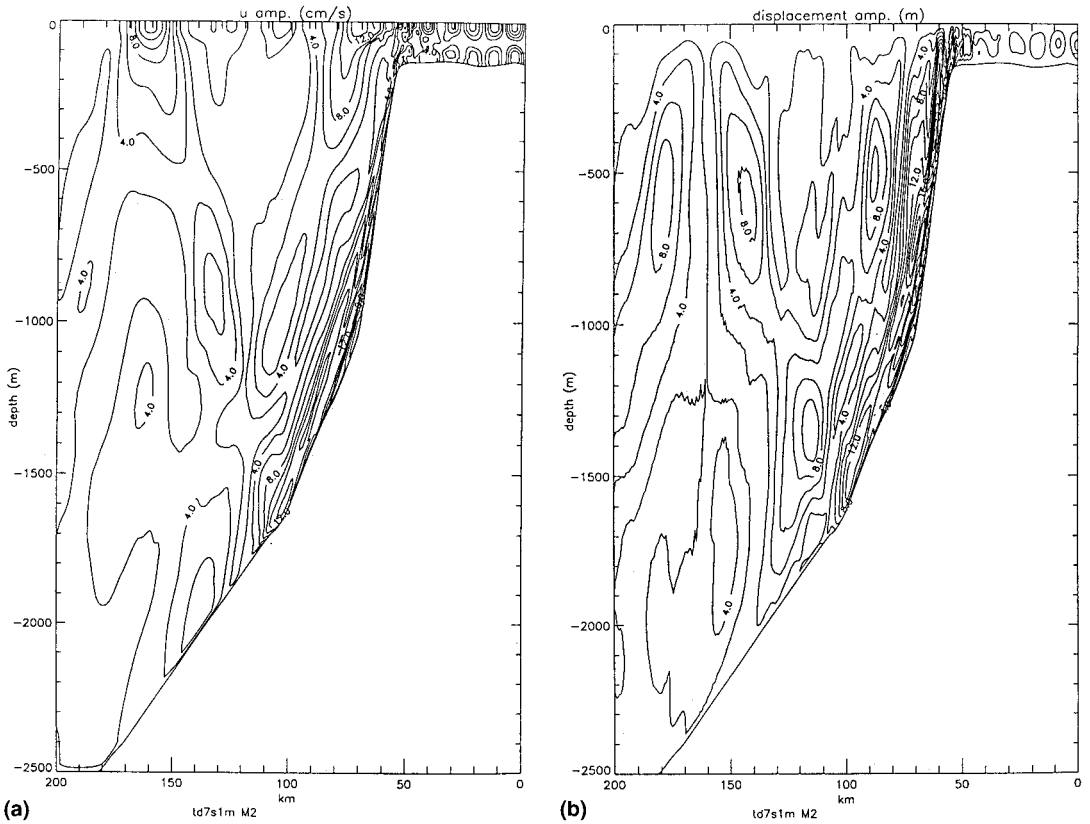

Figure 5. As Figure 4 but without the seamount.

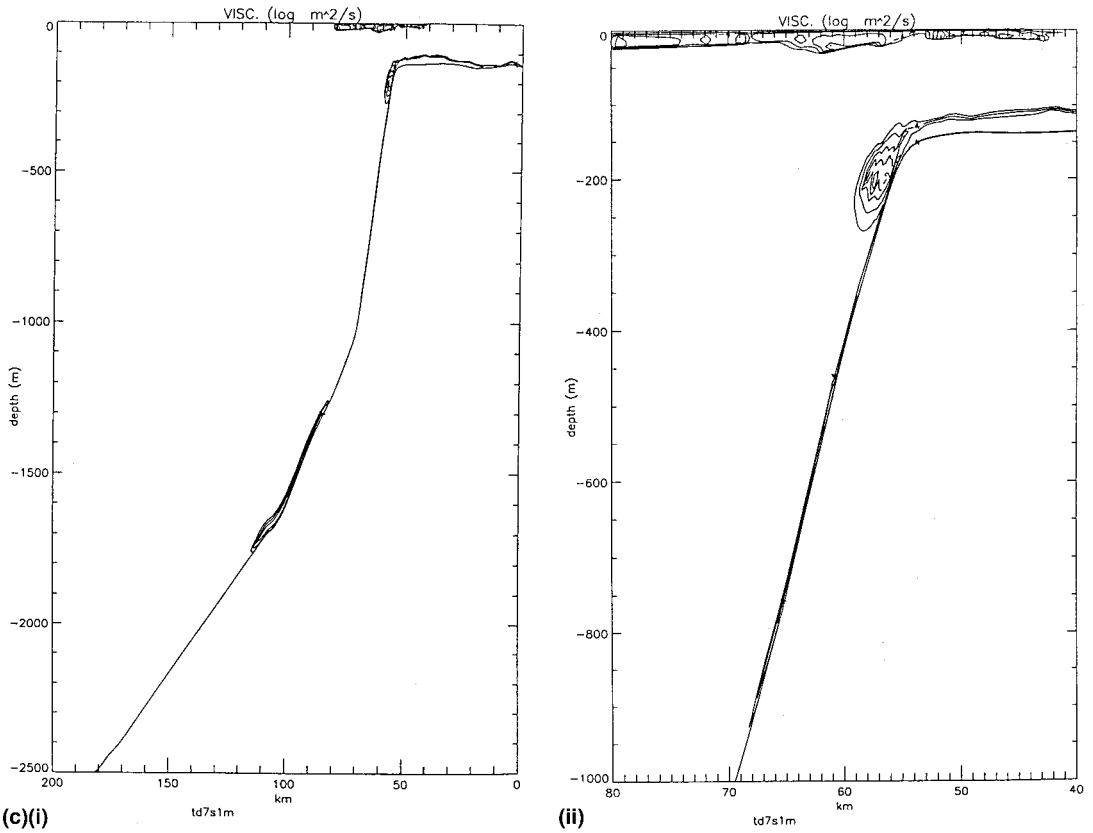

Figure 5 (*Continued*)

(Figure 4(d)). However, away from the shelf slope the density contours are significantly smoother than those obtained previously with no significant disturbance of the near surface σ_t contours appearing at 160 km, suggesting that this disturbance was produced primarily by the seamount.

Contours of the amplitude of the u component of current and the internal displacement at the M_4 frequency (Figure 5(e) and (f)) show that the generation of the higher harmonic in the absence of the seamount is mainly restricted to the upper part of the shelf slope and along the slope. This is different from the calculation with the seamount in which some of the higher harmonic is generated above the seamount (compare Figures 4(e) and (f) and 5(e) and (f)).

The comparison of solutions with and without the seamount clearly shows the importance of the seamount in influencing the propagation of the internal tide away from the shelf slope, and the generation of an internal tide on the seamount slope. Before considering in detail the role of the seamount, by examining it in isolation, we first examine the influence upon the internal tide of small variations in the density profile.

As shown previously (calculations 1 and 2) the change in the density field is slightly different between calculations in which the non-linear terms are included or omitted. Consequently, the change in the M_2 internal tide is not only due to the direct influence of the non-linear terms, but also the change in the density field they produce. Consequently, an examination of variations in the internal tides due to changes in the density field can help explain the results found in previous calculations.

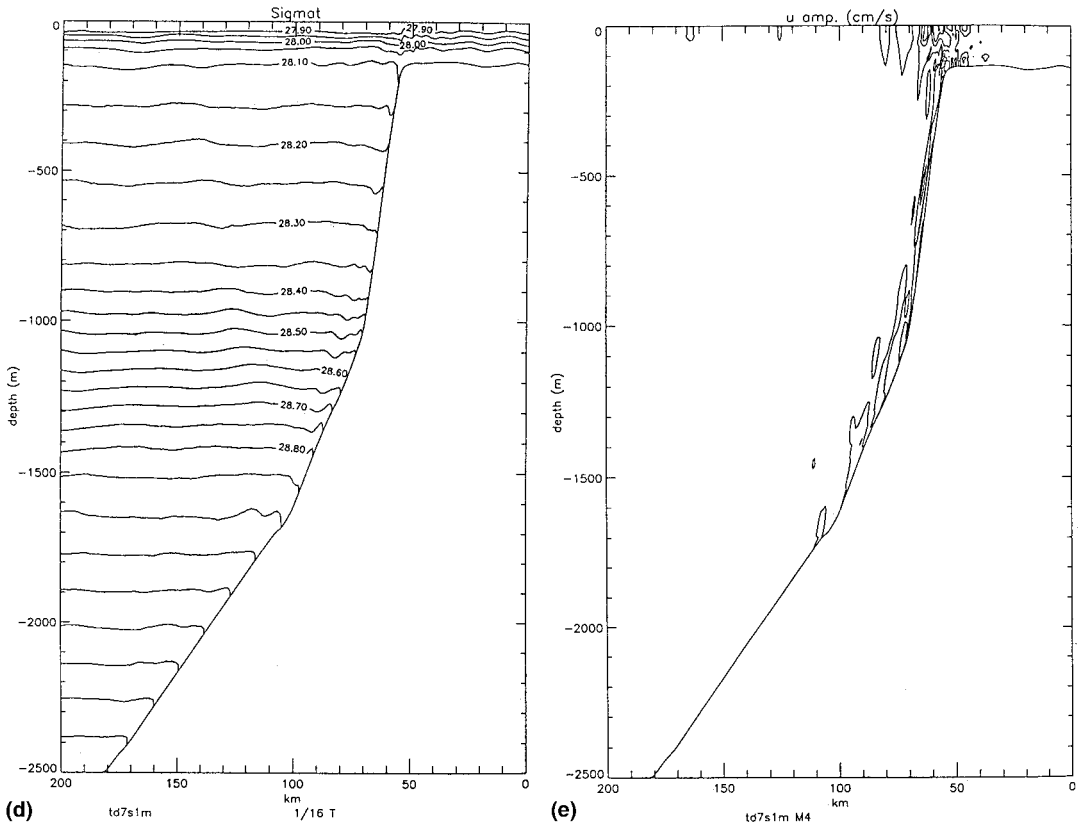

Figure 5 (*Continued*)

3.4. Perturbed winter stratification, with a seamount

In a subsequent series of calculations (Table I, calculations 4 and 5) the change in the solution due to small variations in the density field is examined (which might occur due to the shelf edge flow advecting a slightly different water mass into the area, or due to inaccuracies arising in undersampling the density field). Initially the generation of the internal tide on the shelf slope in the presence of the seamount was examined using the slightly modified winter density field shown in Figure 2 (Table I, calculation 4).

Contours of u current amplitude and internal displacement of density surfaces (Figure 6(a) and (b)) show a mode-two internal tide on the shelf with an increase in near-bed current magnitude at the top of the shelf slope. An increase in current in the near-bed region at approximately 60 km offshore, is also evident (Figure 6(a)), although the spatial distribution is different to that found previously (Figure 4(a)), reflecting differences in the density field. Increased bed currents are also evident on the eastern and western side of the seamount, with the strongest bed currents occurring, as previously, on the eastern side of the seamount (Figure 6(a)). A region of reduced current magnitude is evident above the seamount, with an intensification in surface current magnitude at about 170 km offshore with currents in this region comparable with those found previously (compare Figures 6(a) and 4(a)).

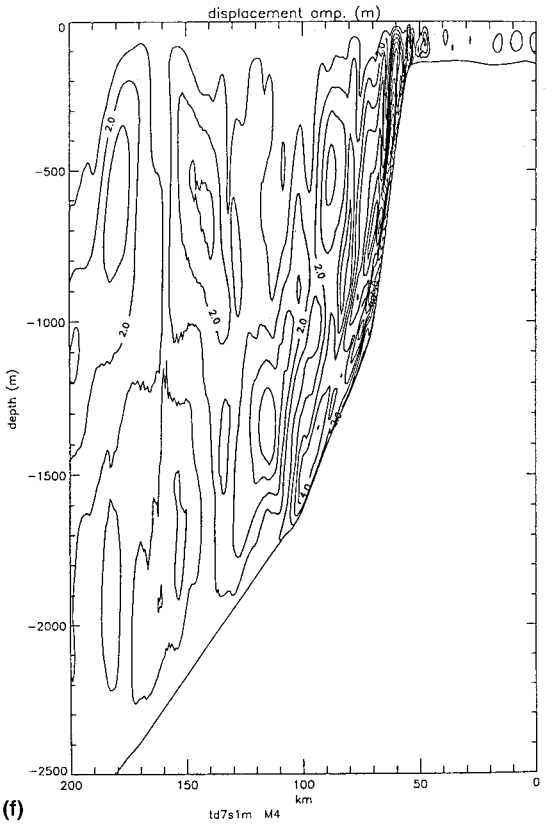

Figure 5 (*Continued*)

3.5. Perturbed winter stratification, without the seamount

Contours of current amplitude and displacement without the seamount (Figure 7(a) and (b)) (Table I, calculation 5) at the top of the slope and on the shelf are not significantly different to those found previously (compare Figures 7(a) and (b) and 6(a) and (b)), although at depths of the order of 1000 m along the slope there is a significant change in the contours of the current amplitude, which show similar features to those computed previously without the seamount (compare Figures 7(a) and 5(a)). However, current contours at this depth at the offshore location where the seamount was previously situated (approximately 140 km offshore) are much smoother and significantly different to those found previously (Figure 5(a)). The intensification of the surface current at approximately 160 km is still present although with a reduced magnitude.

The change in u current amplitude in this series of calculations with the perturbed winter stratification produced by removing the seamount are comparable with those found previously with the winter stratification. Although there are some minor differences in the pattern of u current amplitudes (compare Figures 7(a) and 5(a)) resulting from the differences in the density field, these are small compared with the change produced by modifying the bottom topography to include the seamount. However, both calculations reveal that the internal tide is influenced by the vertical profile of the density field. Also, the change in the density field between the calculations in which the non-linear terms are included or omitted will have had

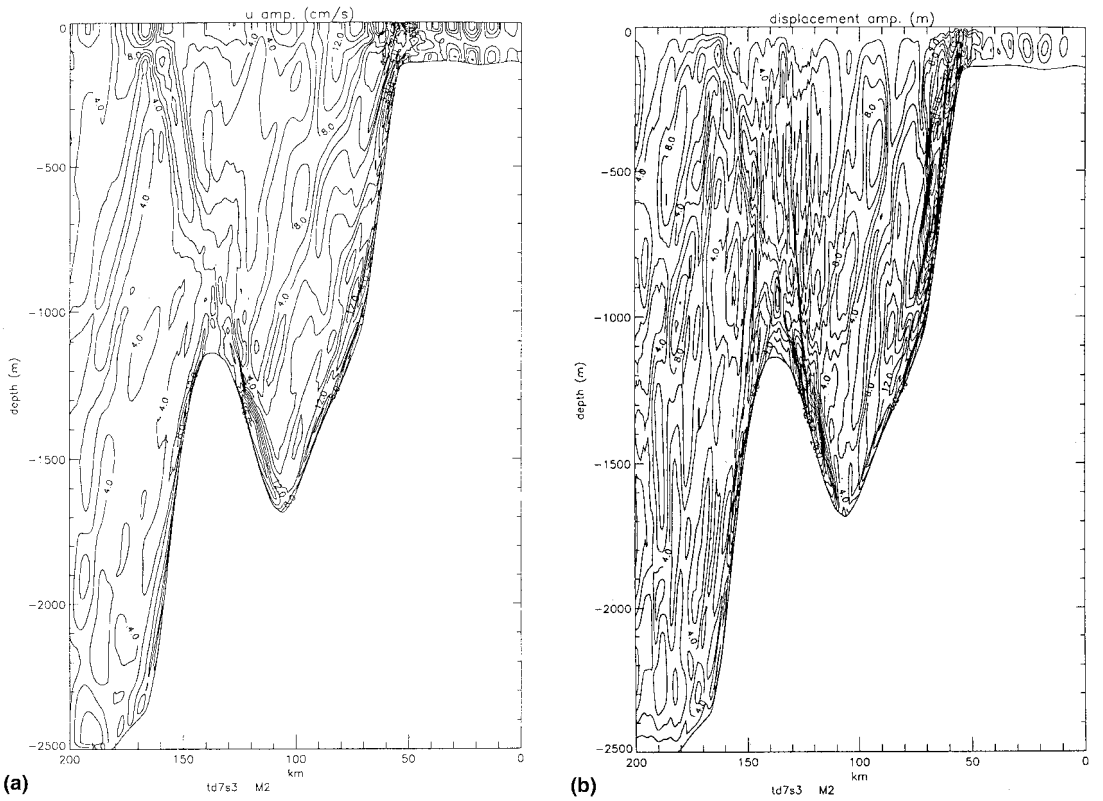

Figure 6. Contours of (a) the current amplitude (cm s^{-1}) and (b) displacement (m) of the M_2 internal tidal current computed with the perturbed winter stratification and the seamount.

an influence upon the internal tide. To examine the effect of the seamount in more detail, the previous calculation was repeated with the slope removed and only the seamount remaining.

3.6. Isolated seamount

In order to examine the role of the seamount in producing a local generation of the internal tide along the seamount slope, it is necessary to consider the seamount in isolation. To accomplish this, water depths to the east of the seamount were fixed at the maximum value found in this area, namely 1700 m, thereby removing the influence of the slope (Table I, calculation 6). Contours of *u* current amplitude (Figure 8) show an intensification of near-bed currents to the west of the seamount comparable with that found previously with the seamount and slope (compare Figures 8 and 6(a)). A similar intensification, although with current magnitude below that found with the slope, is evident in the near-bed currents to the east of the seamount. The reduction in current magnitude on this side of the seamount when the slope is removed is probably due to the fact that when the slope is present internal tidal energy that is generated along the shelf slope, besides propagating towards the shelf, propagates offshore down the slope (Figure 7(a)) and influences the near-bed current on the eastern side of the seamount. Regions of intensified surface current are evident to the west of the seamount at approximately 160 km offshore and to the east of the seamount at approximately 80 km offshore, and to a lesser extent at about 120 km offshore, associated with internal tide

propagation on either side of the seamount as the direction of the tidal flow reverses. The difference in location of these two regions of intensified surface current relative to the top of the seamount arising from the asymmetric nature of the seamount. The region of intensified surface current at 160 km, goes some way to explaining why the surface current at this location is a maximum when both the seamount and the slope are present. Also, the existence of a number of surface maxima to the east of the seamount may explain the complex variations in surface current magnitude in the presence of slope and seamount.

3.7. Summer stratification with seamount and linear model

This section considers the seasonal difference in the internal tide between summer and winter, in order to determine how significant the change in the density profile, due to seasonal effects, is on the distribution of the internal tide, and hence if a different distribution of measurements should be made in summer compared with winter. Also, calculations are performed with and without the non-linear terms in order to determine if the conclusions based upon the winter stratification concerning the importance of these terms is also valid in summer. The summer temperature profile shown in Figure 2 was used with the linear model (Table I, calculation 7).

Contours of the amplitude of the u component of current (Figure 9(a)) show regions of increased near-bed current magnitude near the top of the shelf slope with an intensification at

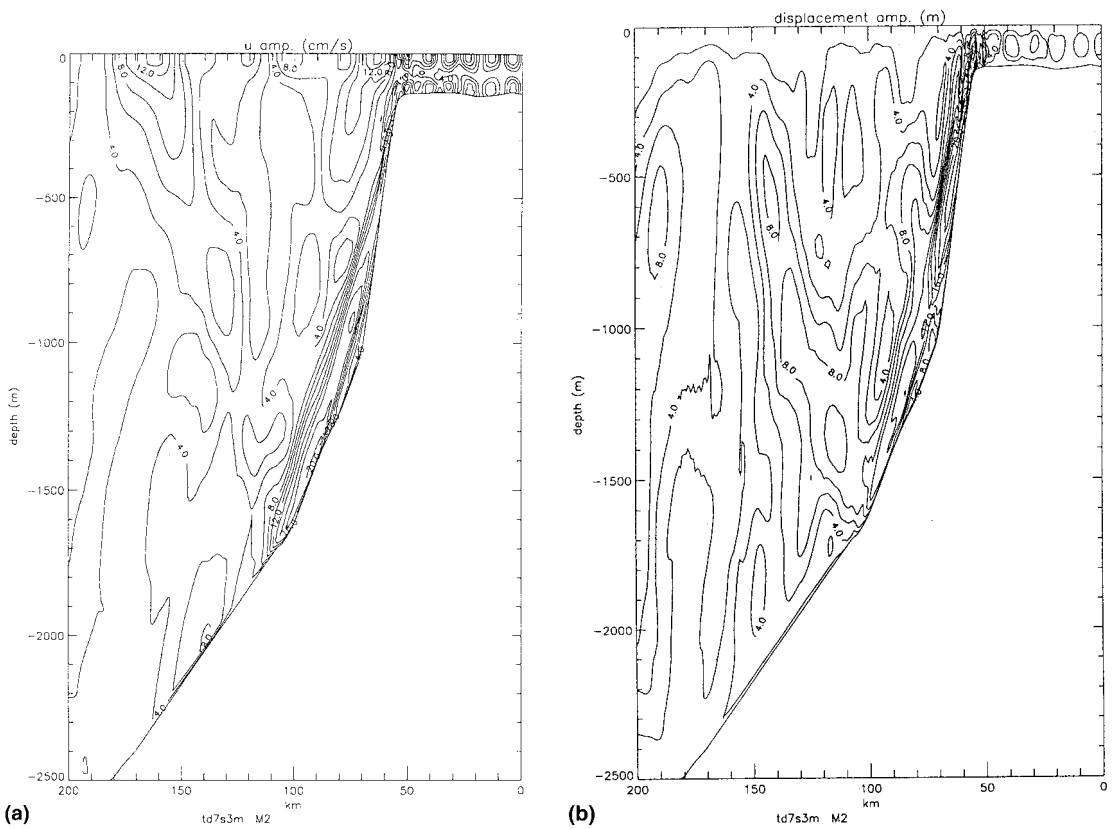

Figure 7. As Figure 6 but without the seamount.

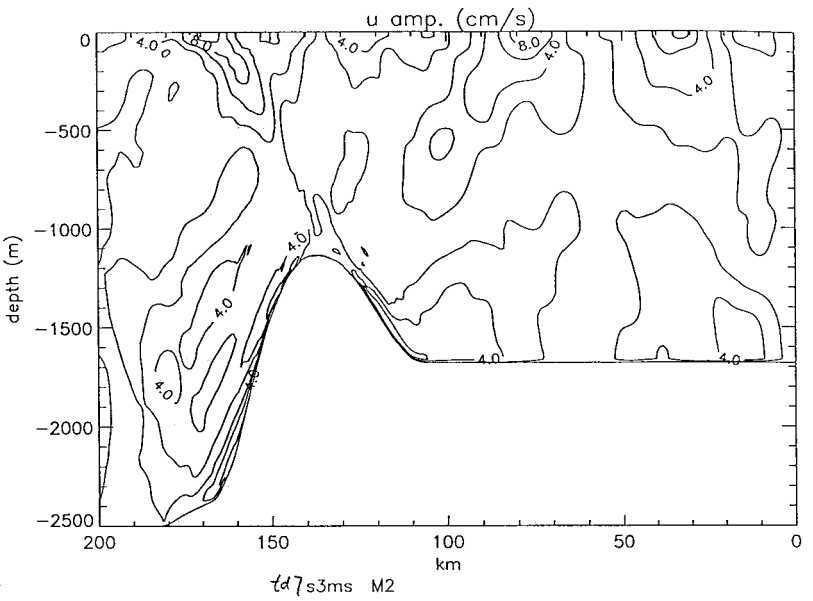

Figure 8. As Figure 6 but with only the seamount.

depth further down the slope, although this intensification is significantly less than that found with the winter stratification (compare Figures 9(a) and 3(a)). Regions of increased bottom current are found on the western and eastern side of the seamount although again these are not as intense as those occurring with the winter stratification.

Contours of internal displacement (Figure 9(b)) show similar patterns to those found previously with a region of very strong internal displacement occurring at the top of the shelf break. Although areas of significant internal displacement occur in the near-bed region to the east and west of the seamount, the magnitude of this internal displacement is significantly less than in the winter time. Also, the region of strong internal displacement above the seamount is no longer evident.

The most significant difference between the summer and winter situations is the existence of regions of intensified surface currents extending from the shelf break out into the ocean in the summer time, whereas in the winter only two regions are present, namely the one at 70 km from the coast and the second at 160 km separated by an area of smaller currents. Regions of intensified surface current are also present on the shelf in summer time although limited to the shelf edge adjacent to the top of the shelf break in winter. The effect of this region of high near-surface current shear in the summer time is to increase turbulence production over the whole area.

Differences in the spatial distribution of turbulence energy and viscosity at the top of the shelf slope where they are a maximum can be seen from a detailed comparison of Figure 9(c) and (d) with Figure 3(c). (Note that in Figure 9(c) and (d) only a subdomain of the region, namely the top of the shelf slope, is plotted.) In the summer time the region of sheared surface currents extends from shelf to ocean, giving rise to the surface layer of enhanced turbulence energy and viscosity shown in Figure 9(c) and (d). At the sea bed at the top of the shelf, an area of increased turbulence energy and viscosity arises in the summer.

Contours of the density surfaces (an instantaneous picture after 30 tidal cycles at the top of the shelf slope) (Figure 9(e)) show a surface layer over which σ_t changes very rapidly, associated with the existence of the near-surface thermocline, which is present at this time of the year. Disturbances of the density surfaces produced by internal waves are clearly evident on the thermocline. Enhanced mixing in the bottom layer of the shelf associated with tidal turbulence gives rise to the thicker bottom layer to the east of 48 km, giving rise to the intersection of the $\sigma_t = 28.10$ surface and the sea bed. A similar situation occurs in the winter time, however at this time of year the $\sigma_t = 28.10$ surface is at a greater depth and upwells at the top of the shelf break (Figure 3(d)). Upwelling at the shelf break of the $\sigma_t = 28.15$ and 28.20 surfaces is clearly evident in Figure 9(e) due to the internal tide.

3.8. Summer stratification with seamount and non-linear model

Contours of the *u* current amplitude (Figure 10) computed with the same initial conditions but with the inclusion of the non-linear momentum terms (Table I, calculation 8), show significantly larger spatial variability than those computed with the linear model (Figure 9(a)). The larger spatial variability is due to the fact that the non-linear terms can generate higher tidal harmonics with shorter wavelengths than the fundamental. The increase in spatial

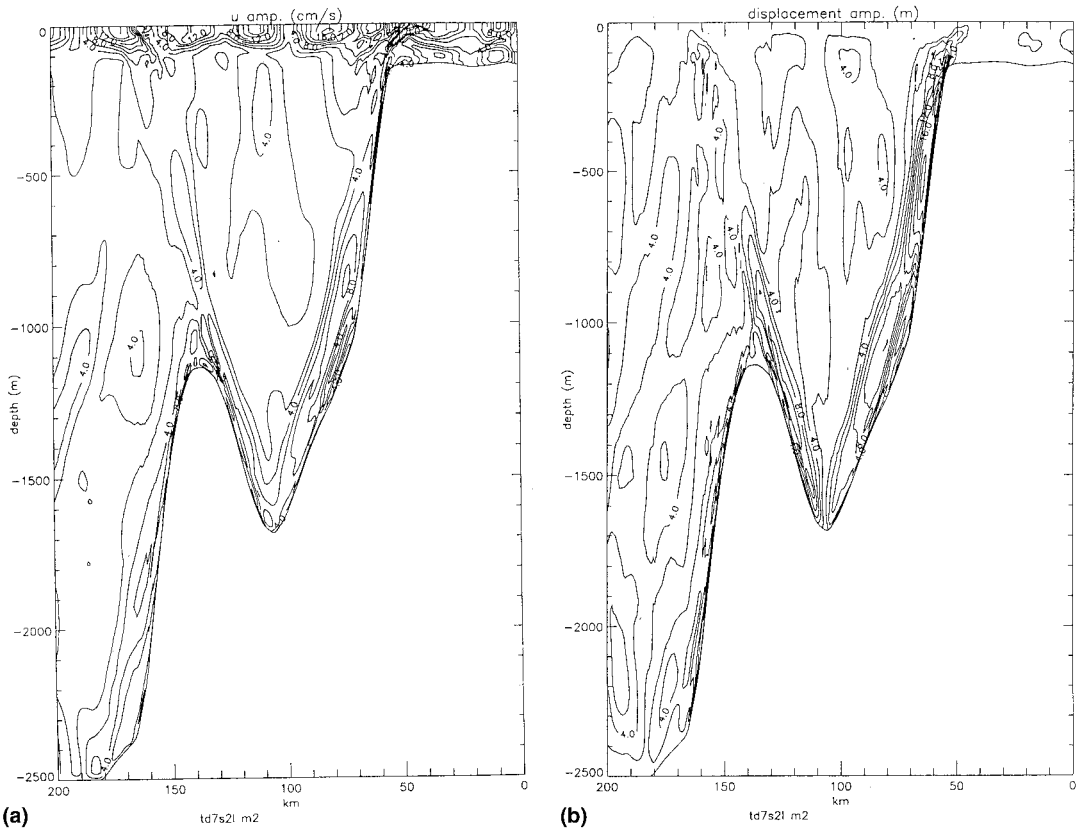

Figure 9. Contours of (a) the amplitude (cm s^{-1}) of the internal tidal current, (b) the internal displacement (m) at the M_2 frequency, (c) turbulence energy ($\log_{10}$ m^2 s^{-1}), (d) viscosity ($\log_{10}$ m^2 s^{-1}) mean over an M_2 tidal cycle, (e) instantaneous values of σ_t, computed with the linear model and summer stratification.

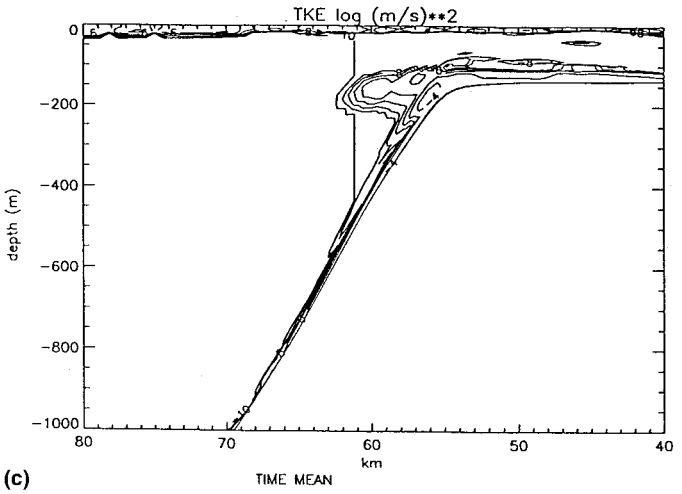

(c)

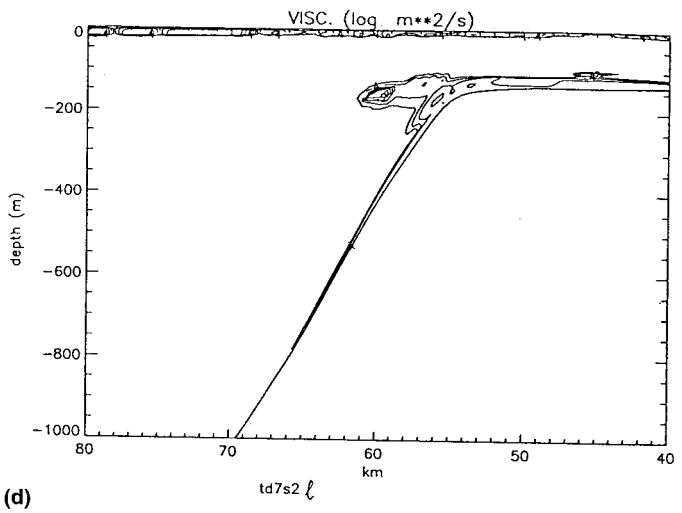

(d)

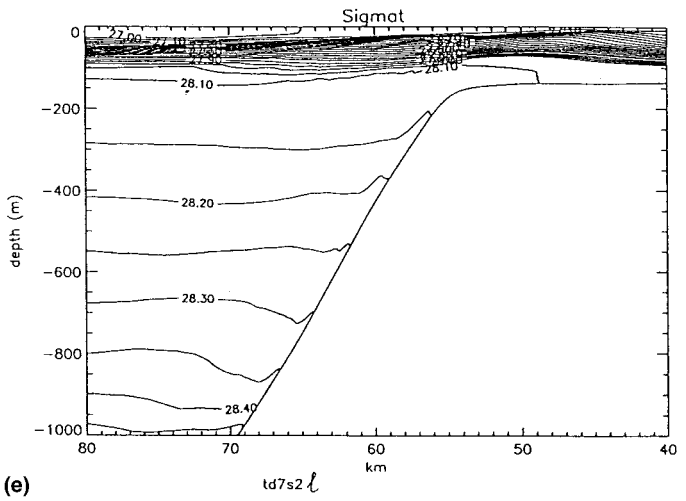

(e)

Figure 9 (*Continued*)

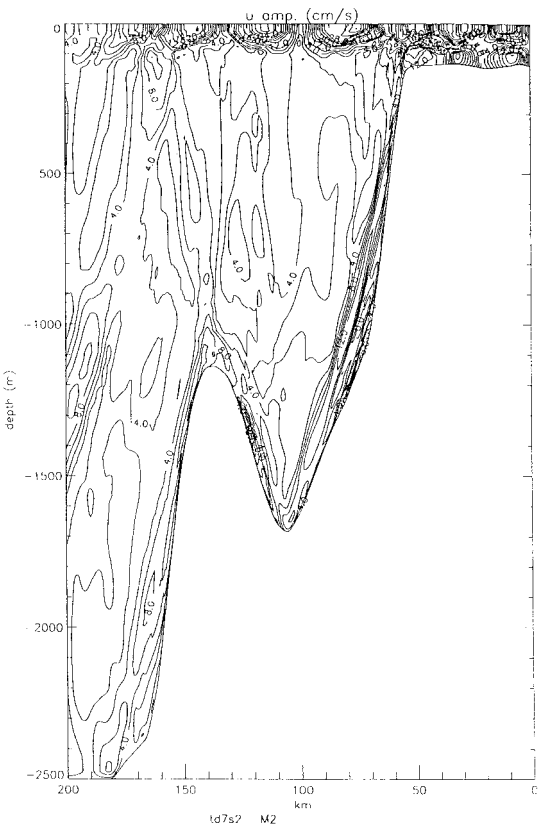

Figure 10. As Figure 9(a) but computed with the non-linear model.

variability found with the non-linear model compared with the linear model is consistent with that found with the winter stratification and emphasizes the importance of retaining the non-linear terms in any three-dimensional model. The seasonal variability found in the internal tide suggests that observations in both winter and summer would be a test of the ability of a model to reproduce seasonal variations in the internal tide. The significantly larger spatial variability found in the surface layer in the summer time suggests that observations at this time of year should be concentrated in the upper part of the water column.

4. INTERNAL TIDE CALCULATIONS AT 57°N (INFLUENCE OF BOTTOM MIXING AND SHELF EDGE TOPOGRAPHY)

As stated previously, an intense measurement programme is planned to take place across the shelf slope off the west coast of Scotland (Figure 1(a)), and the objective of the calculations presented here is to examine the detail of the structure of the internal tide in the region with a view to determining the influence of topography and a bottom mixed layer, upon the internal tide. In the previous section, the influence of a topographic feature, namely a seamount on the internal tide generation at 56.5°N was considered. This section examines another location in the region of interest, namely 57°N using the same cross-shelf model. At this location there is

no seamount and the shelf slope is different from that used previously. In an initial series of calculations using the non-linear model, the influence of changes in the density profile in the near-bed region due to cascading of cold shelf water upon the internal tide using the same shelf slope topography as that employed in [9] is examined. If the existence of a pool of cold well-mixed water at depth has a significant influence upon the internal tide in the upper part of the water column, then it will be necessary to make observations in the near-bed region to determine the existence of such water masses. Also since the cascading of cold water is an episodic event, then it may be responsible for observed near-surface sudden changes in the internal tide, if it has an influence away from the near-bed region.

4.1. Influence of the presence of a bottom mixed layer upon the internal tide

In the first calculation (calculation 9) at 57°N the density profile typical of a winter time situation (Figure 2) (linearly extrapolated to the sea bed) was used in the vertical. In a subsequent calculation (calculation 10, see later) the density field below 1400 m was modified to represent a well-mixed oceanic bottom boundary layer.

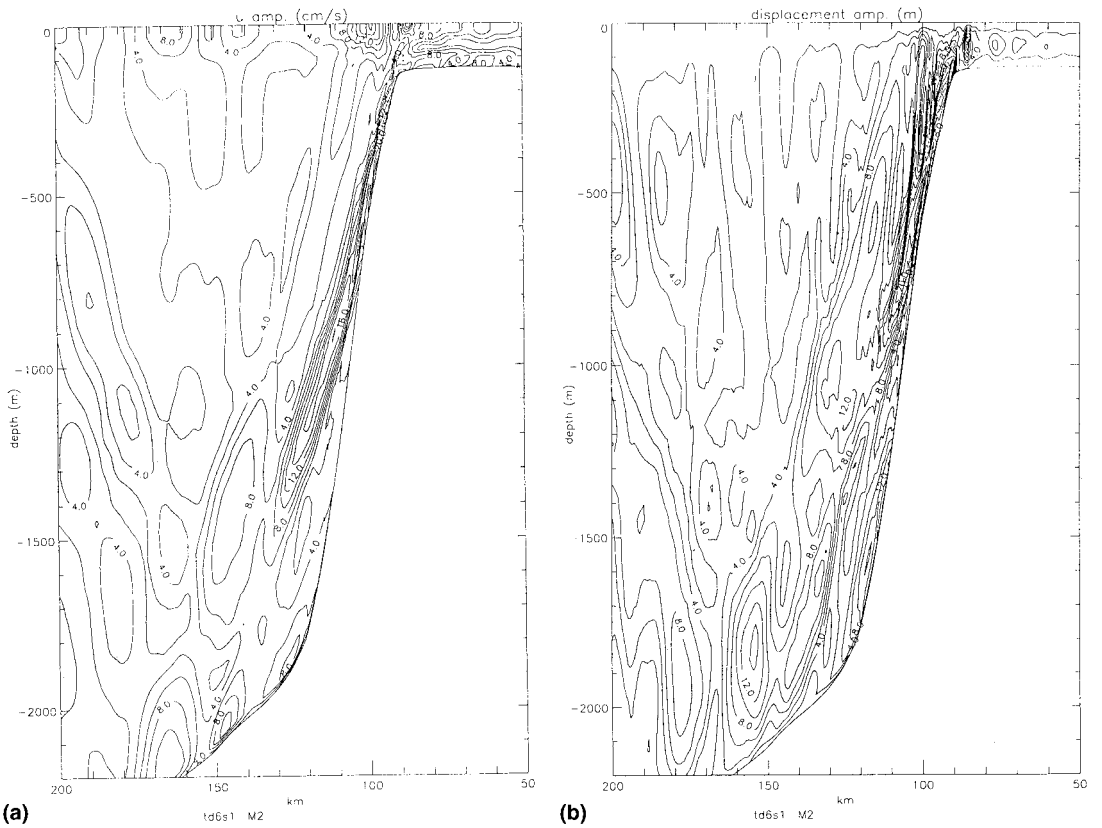

Figure 11. Contours of (a) the amplitude (cm s^{-1}) of the internal tidal current, (b) the internal displacement (m) at the M_2 frequency, (c) the amplitude (cm s^{-1}) (at the top of the shelf edge) and (d) the internal displacement (m) at the M_4 frequency, (e) the amplitude (cm s^{-1}) and (f) the displacement (m) at the M_6 frequency (g) contours of time-averaged turbulency energy ($\log_{10}$ m^2 s^{-2}) (h) contours of time average viscosity ($\log_{10}$ m^2 s^{-1}) (i) contours of energy flux (W m^{-2}) and spatial distribution of the depth integrated energy flux (W m^{-1}).

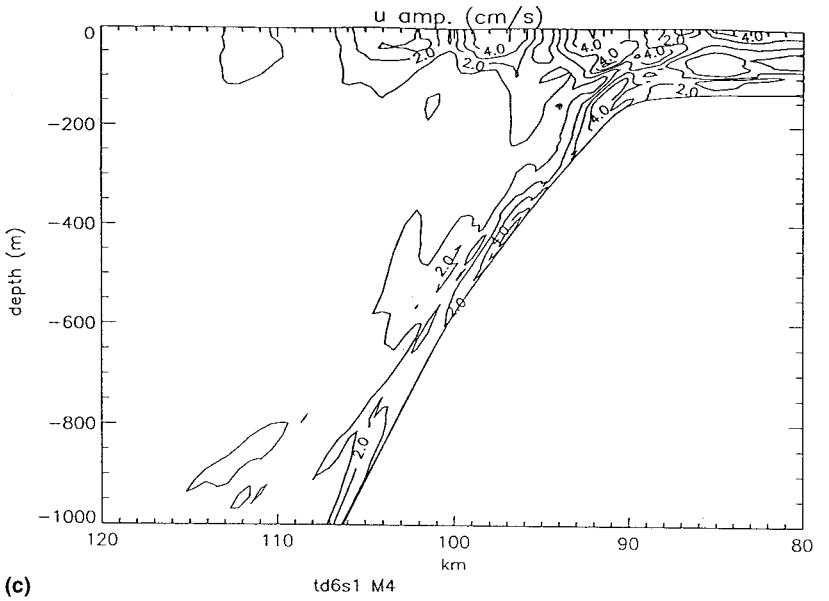

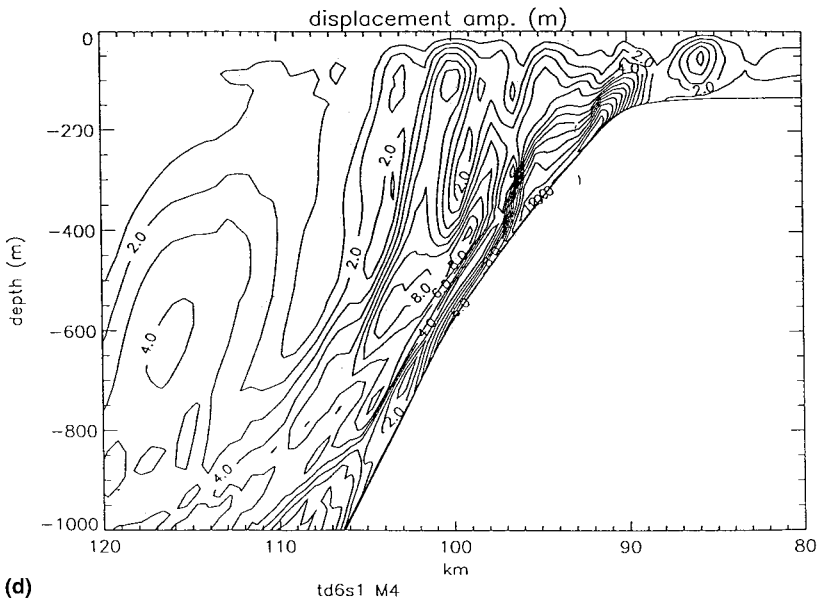

Figure 11 (*Continued*)

Contours of u current amplitude and displacement (Figure 11(a) and (b)) [note that since we are primarily interested in the shelf slope region, we do not plot the region close to the coast] at the M_2 frequency computed using the typical winter density profile (calculation 9) show an intensification of the current and displacement at the top of the shelf break with a region of intensified currents above the shelf slope extending from the shelf break to a depth of 1500 m. Away from the shelf slope a region of enhanced currents extending upwards and westward from a depth of 1500 m about 170 km offshore up to a depth of 500m at 200 km is evident,

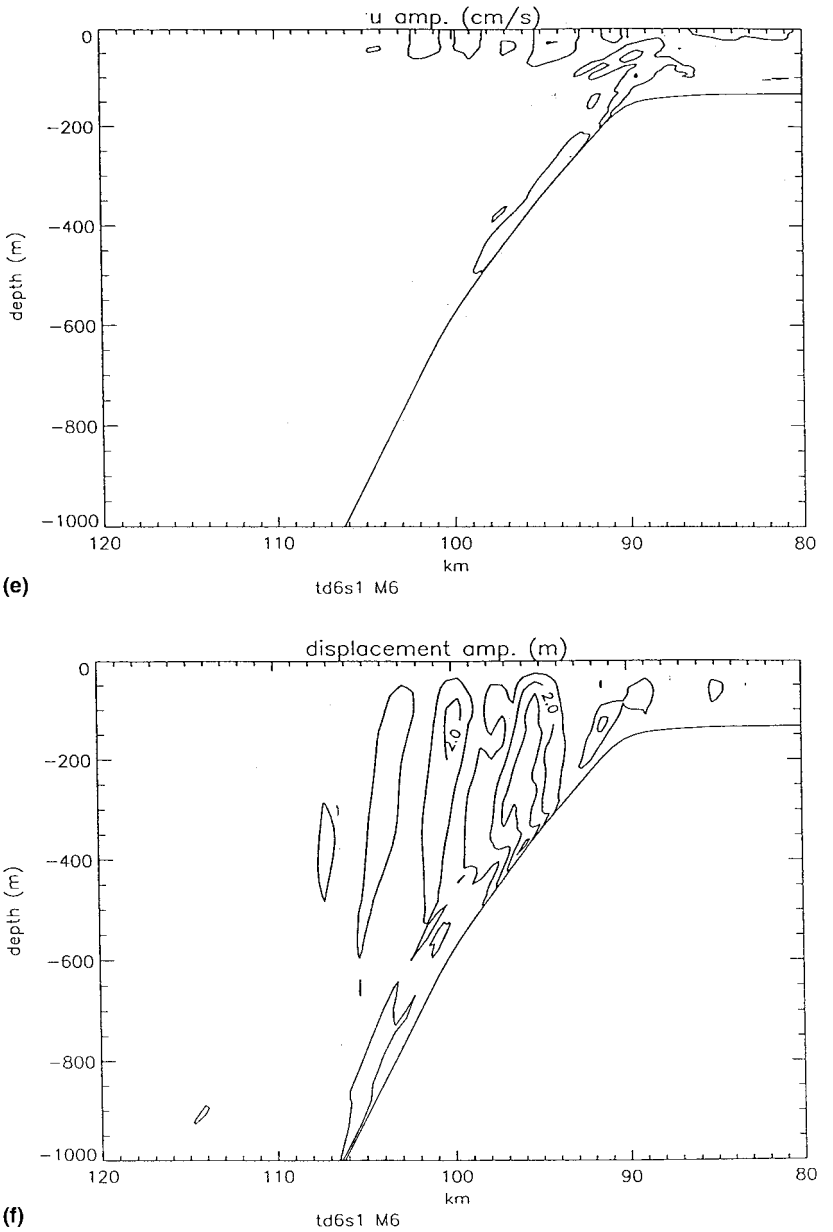

Figure 11 (*Continued*)

associated with a bottom reflection of the internal tide. Regions of intensified surface current are evident to the west of the top of the shelf slope (at 100 km offshore) and at about 160 km offshore, associated with the propagation of the internal tide along ray paths [5,8]. Contours of internal tide displacement (Figure 11(b)) at the M_2 frequency show large internal displacements (of order up to 28 m) in the shelf slope region.

Internal tidal currents and displacements at the M_4 frequency (the second higher harmonic of M_2, and generated by non-linear interaction) near the top of the shelf slope (Figure 11(c)

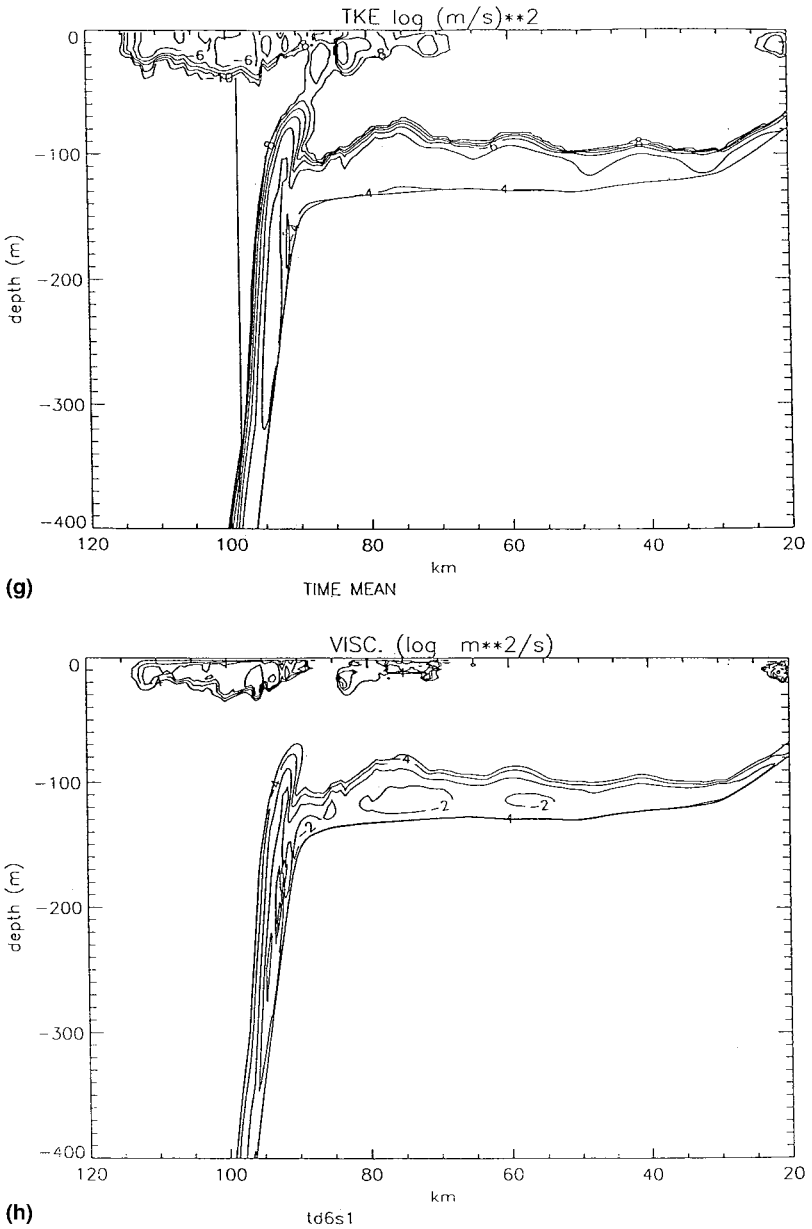

Figure 11 (*Continued*)

and (d)) [note only a limited region is plotted here] show that the higher harmonic of the tide is primarily generated at the top of the shelf slope where the non-linear term is large giving rise to M_4 internal tidal current amplitudes of the order of 4 cm s^{-1} and displacements of order 10 m. Contours of current amplitude and displacement at the M_6 frequency (the third higher harmonic of M_2) are mainly confined to the upper part of the slope and shelf break with current magnitudes of order 2 cm s^{-1} (Figure 11(e)) and displacements of 4 m (Figure 11(f)). Contours of turbulence energy and viscosity (Figure 11(g) and (h)) show regions of enhanced

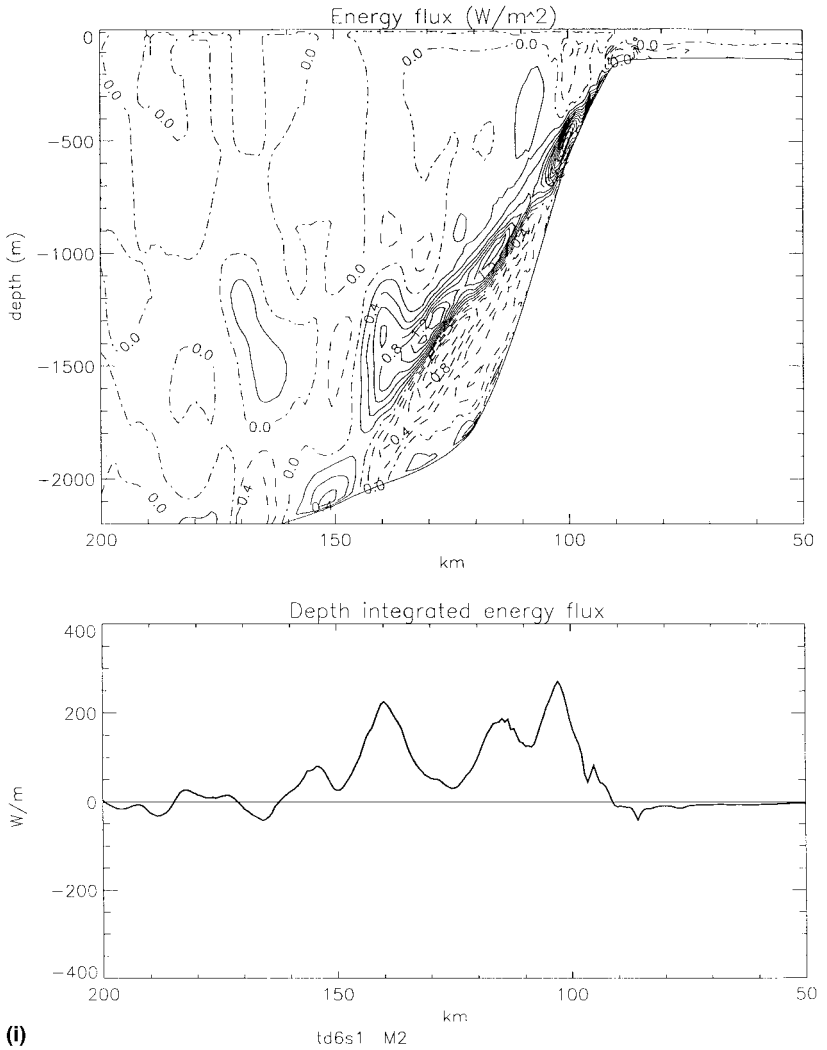

Figure 11 (*Continued*)

turbulence energy at the top of the shelf break and in the surface layer above this, due to the increased shear production of turbulence in these regions associated with the enhanced currents. This increase in turbulence energy gives rise to a maximum in the eddy diffusivity (not shown) and viscosity (Figure 11(h)) in these regions. Contours of internal tidal energy flux and its depth mean value, computed as in [37], are given in Figure 11(i) and will be discussed later.

In a subsequent calculation (Table I, calculation 10), the winter temperature profile (Figure 2) was modified by linearly interpolating the temperature to 1400 m, with a constant temperature region below this, corresponding to a well-mixed bottom boundary layer ($N^2 = 0$) below 1400 m was used. This profile effectively giving a density front at 1400 m with a well-mixed layer below. This cool well-mixed region may be thought of as arising from cold water cascading down the shelf slope.

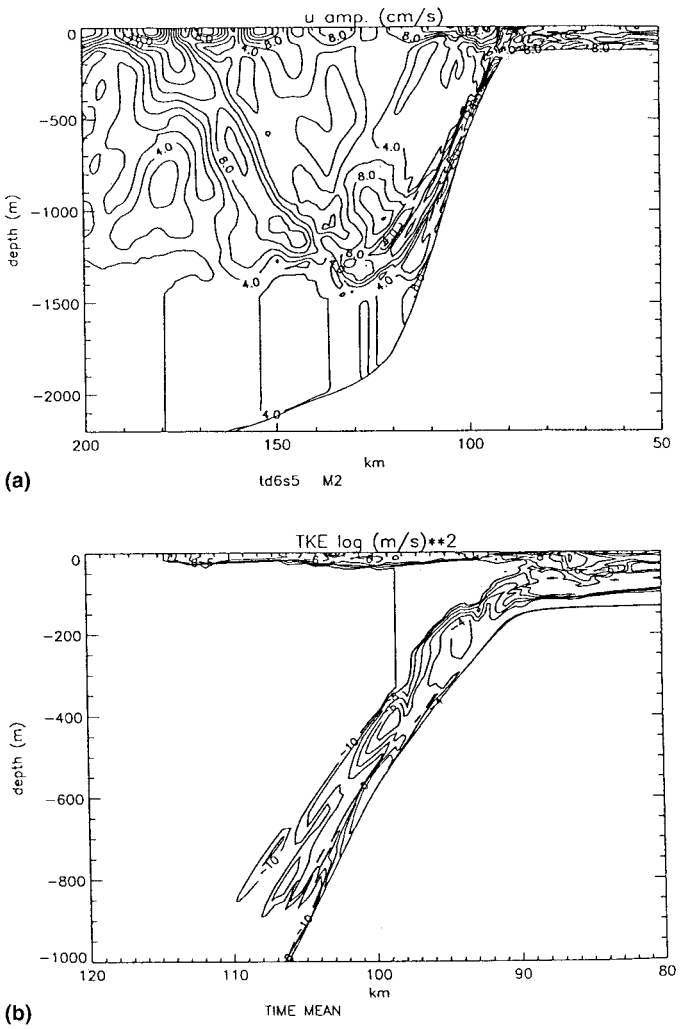

Figure 12. Contours of (a) the amplitude ($cm\,s^{-1}$) of the internal tidal current, (b) contours of time-averaged turbulence energy ($\log_{10} m^2\,s^{-2}$) (at the top of the shelf) (c) contours of time-averaged eddy viscosity ($\log_{10} m^2\,s^{-1}$) (at the top of the shelf). (d) Contours of energy flux ($W\,m^{-2}$) and spatial distribution of the depth integrated energy flux ($W\,m^{-1}$), computed with the temperature profile corresponding to a well-mixed near-bed region.

Contours of u current amplitude at the M_2 frequency (Figure 12(a)) show an intensification of current at the top of the shelf slope in the near-bed and near-surface layer, which is similar to that found previously (Figure 11(a)) with the region of intensified currents above the shelf slope only extending down to 1400 m at a location approximately 130 km offshore. Below 1400 m the spatial distribution of u current contours is significantly different to that found previously and does not show any regions of local intensification at the bed suggesting that internal tidal energy is being reflected by the density change occurring at 1400 m. (This point will be discussed later in more detail.) A region of intensified current amplitude, extending upwards and offshore from the position at 130 km offshore and depth of 1400 m can be readily seen in Figure 12(a). The location and intensity of this region is significantly different from that found previously (Figure 11(a)), again suggesting a different ray path of internal

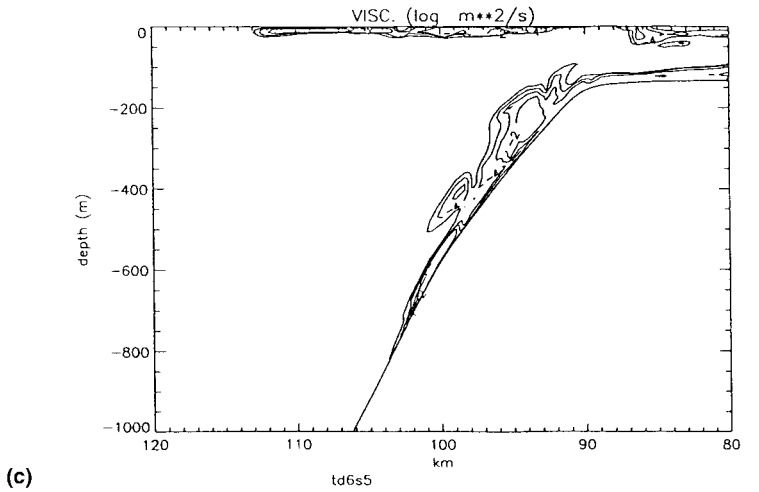

(c)

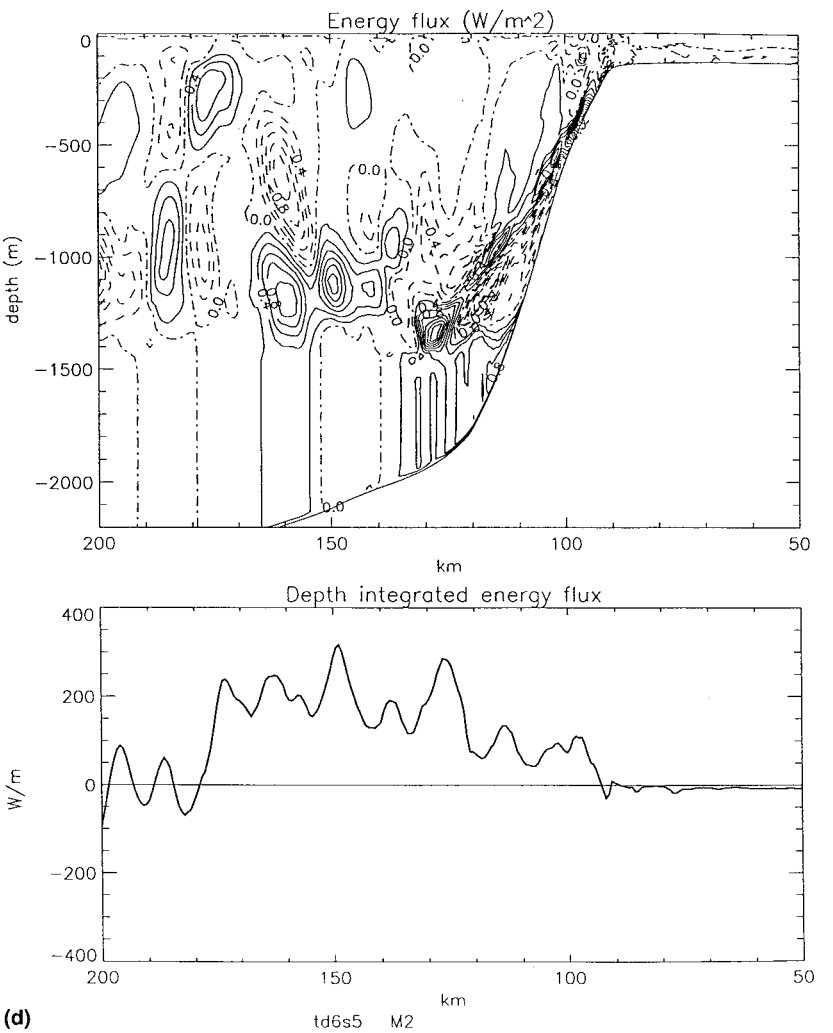

(d)

Figure 12 (*Continued*)

energy transmission, due to the reflection of internal tidal energy by the density surface. The spatial distribution of regions of intensified surface current is also significantly different to that found previously, suggesting the reflection of internal energy at the density interface rather than along the slope and at the sea bed as in the previous case (Figure 11(a)).

Contours of turbulence energy and eddy viscosity at the top of the shelf break (Figure 12(b) and (c)) (note that only the top of the shelf slope is plotted) show a region of slightly increased mixing compared to that found previously (Figure 11(g) and (h)) due to the differences in the density field at depth. This change in mixing will influence the local density field at the top of the shelf break, which may influence the energy flux.

Contours of internal tide energy flux (Figure 12(d)) (domain plotted is identical to that given in Figure 12(a)) show a region of strong energy flux near the top of the shelf break, with the maximum slightly closer to the top of the shelf (Figure 12(d)) than in the previous case (Figure 11(i)). The reasons for this difference is probably due to the differences in density arising from different mixing rates as shown above. Contours of the energy flux between 100 and 140 km offshore, show a region of maximum energy flux above the slope extending down to 1400 m depth but falling to a very small value below this (Figure 12(d)) suggesting a reflection of energy at 1400 m. This is different from the contours of energy flux found previously where the flux extends below 1800 m, with a region of bed flux at 150 km offshore. Contours of energy flux to the west of 140 km offshore, show a significant energy flux is present in this region compared with the previous calculation (Figure 11(i)) where the energy flux rapidly decays to near zero offshore of 140 km.

The significant differences found between calculations 9 and 10 clearly show that slight differences in density distributions at depth can change the spatial distribution of the internal tide due to reflection of the internal tidal energy. This reflection gives rise to a significant increase in the strength of the internal tide at offshore locations, in particular the surface current and the turbulence mixing associated with these regions of increased current. This suggests that it is important to determine the density field at depth, if the detailed spatial variability of the near surface internal tide is to be modelled. Also any major changes in the near-bed density field produced by the cascading of cold water will give rise to significant changes in the near-surface internal tide.

4.2. Influence of shelf slope topography upon the internal tide

In the previous series of calculations a fine grid model of resolution 0.625 km was used, with topography based upon interpolating the water depths from the three-dimensional barotropic model of Xing and Davies [14], which used a grid of order 4 km (Figure 1(b)). The depths in this model were derived from navigation charts of the region, which gave point depths at locations ranging from 4 km up to 10 km apart, which were then interpolated to provide average depths over a 4 km grid. In the absence of a detailed survey this was the best depth distribution available. The finer grid (0.625 km) was required to accurately reproduce the rapid changes in the density field in the shelf break region produced by the non-linear terms [9]. However, since the water depths were no better than those used in the coarse grid model, fine details of the topography were not resolved. Also, as we will show, the fact that the depths in the model were based upon coarsely spaced point depths, produced a depth distribution that not only failed to include small-scale chances in the shelf slope, but also failed to accurately represent the steepness of the slope. Recently, a detailed shelf edge survey has been carried out [13] leading to a significant improvement in water depth distribution, which has now been included into the 0.625 km grid, giving a model with a more accurate topography (calculation

11). The influence of the more accurate topography upon the steepness of the shelf slope can be clearly seen by comparing the water depth distributions in Figures 13(a) and 11(a). For example, in Figure 13(a) the water depth 100 km from the coast is about 1000 m, whereas in Figure 11(a), it is of the order of 600 m, with a water depth of 1000 m occurring at about 105 km from the coast. The fact that the water depth of 1000 m occurs 5 km further offshore in the interpolated/coarser depths is due to the lack of detailed depths on the original charts used to derive this data, as discussed previously. Also, at a depth of 1600 m and a number of other depths, the depth distribution from the survey shows a small local change in shelf slope (Figure 13(a)) that was not present in the depths derived from charts (Figure 11(a)).

Although the depth distributions shown in Figures 11(a) and 13(a) are different, these differences are significantly less than those between line 56.5°N (the location of the seamount) and the present location, and hence it is useful to consider how these smaller differences in topography influence the internal tide. This is particularly important in determining the accuracy of internal tide predictions in other regions, in that in the absence of a detailed survey (which is not generally made), a somewhat inaccurate depth distribution would have to be derived from charts.

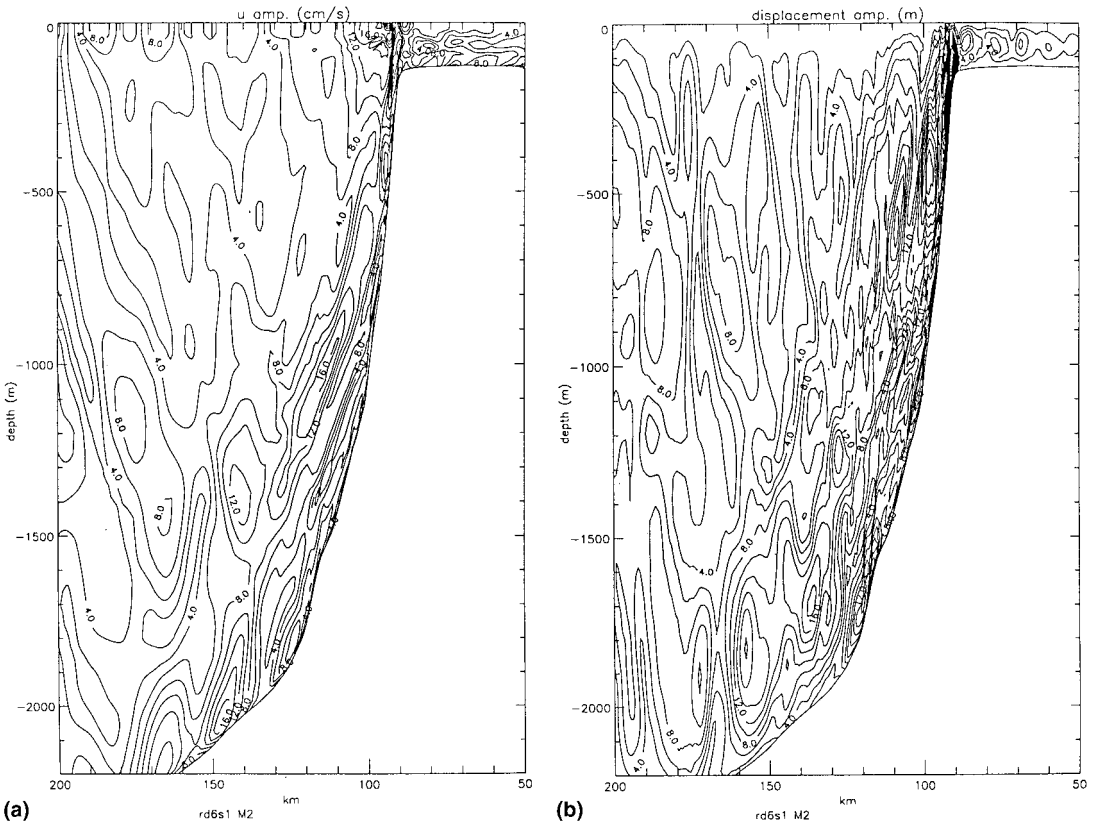

Figure 13. Contours of (a) the amplitude (cm s^{-1}) of the internal tidal current, (b) the internal displacement (m) at the M_2 frequency (over the whole region) (c) the amplitude (cm s^{-1}) (at the top of the shelf slope) and (d) the internal displacement (m) at the M_4 frequency, (e) the amplitude (cm s^{-1}) and (f) the displacement (m) at the M_6 frequency, (g) contours of time averaged turbulence energy ($\log_{10}$ $m^2 s^{-2}$) and (h) contours of time average viscosity ($\log_{10}$ $m^2 s^{-1}$) computed with high resolution topography.

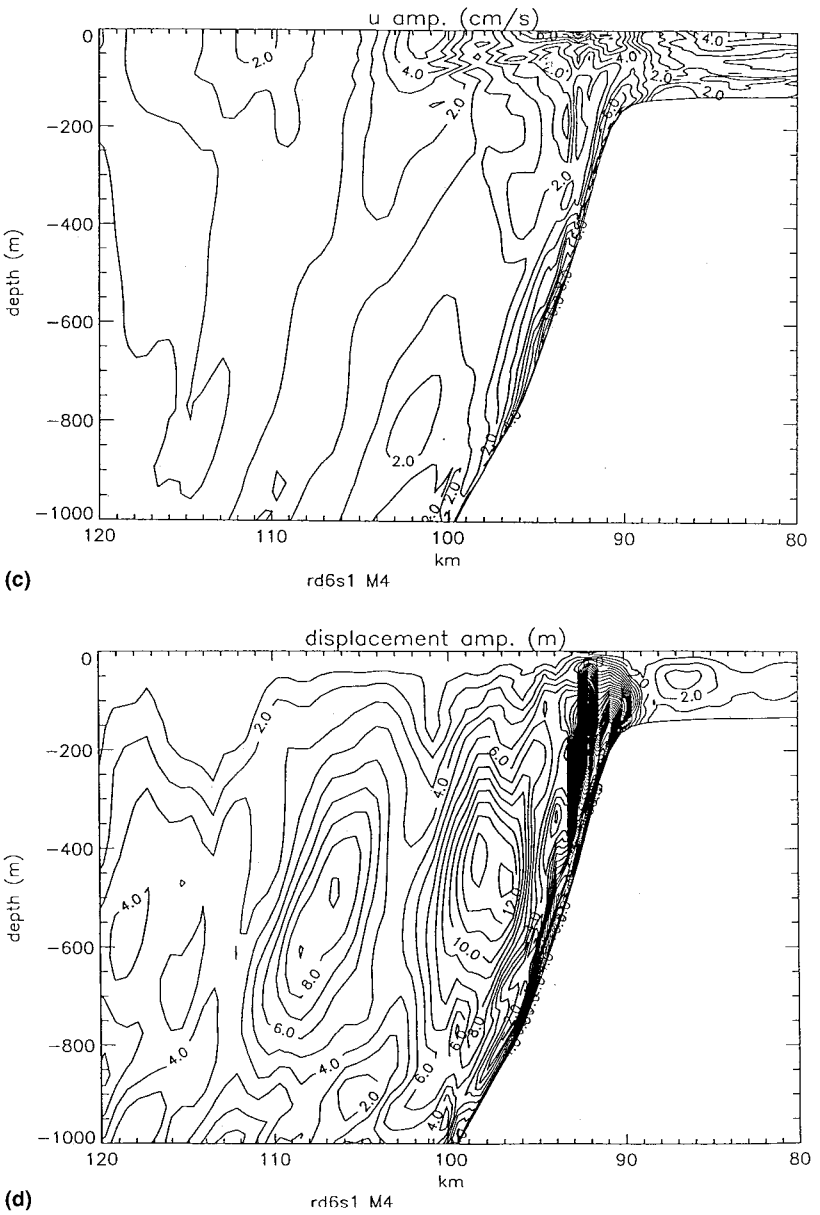

Figure 13 (*Continued*)

Computed contours of M_2 u current magnitude (Figure 13(a)) using the same initial density field as that in calculation 9, but with the improved topography, show a similar shelf distribution of u current amplitude, although the spatial distribution of contours at the top of the shelf break is significantly different, reflecting the steeper gradient of the shelf slope in the present model (compare Figure 13(a) and 11(a)). A region above the shelf slope where currents reach a maximum of 16 cm s^{-1} is evident at a depth of 1000 m (Figure 13(a)), with a similar maximum, although much closer to the bed occurring with the coarser topography (Figure

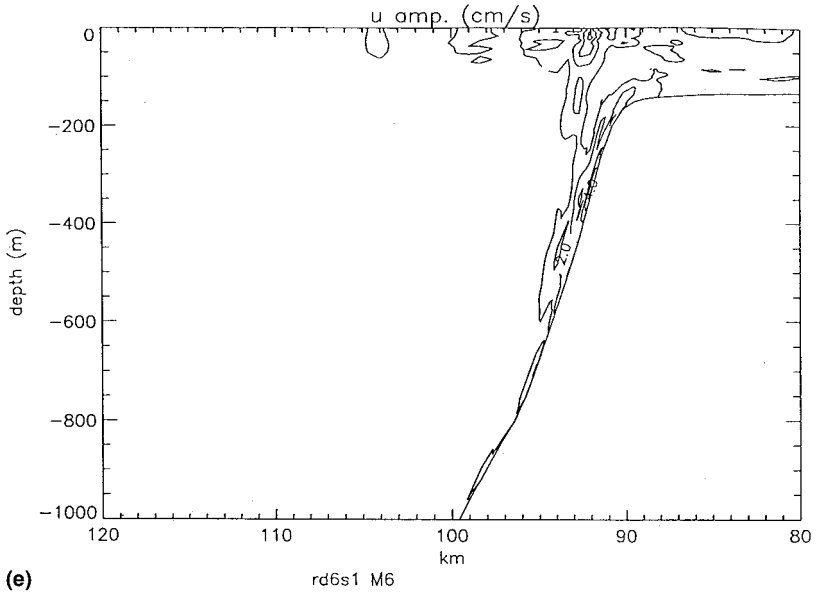

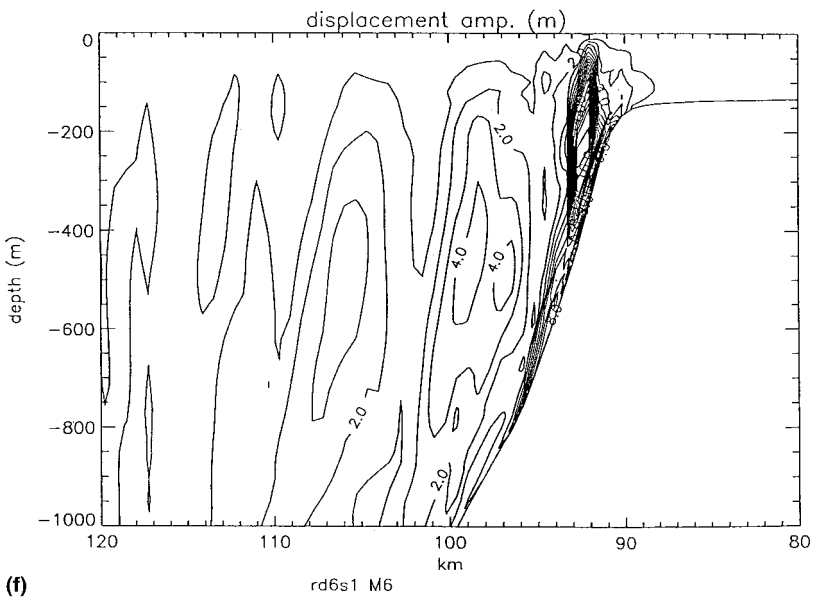

Figure 13 (*Continued*)

11(a)). The differences in the near-bed region down the slope where there are a number of areas of strong bed current (Figure 13(a)) that are not present in calculation 9 appears to arise from the fact that the higher resolution topography does not have the uniform slope used previously but contains a number of locations where the local slope changes from the average slope associated with the shelf edge. These local variations in topography generate local internal tides at positions where the bottom slope and density gradient reach subcritical or supercritical values giving rise to internal tides propagating in different directions. These

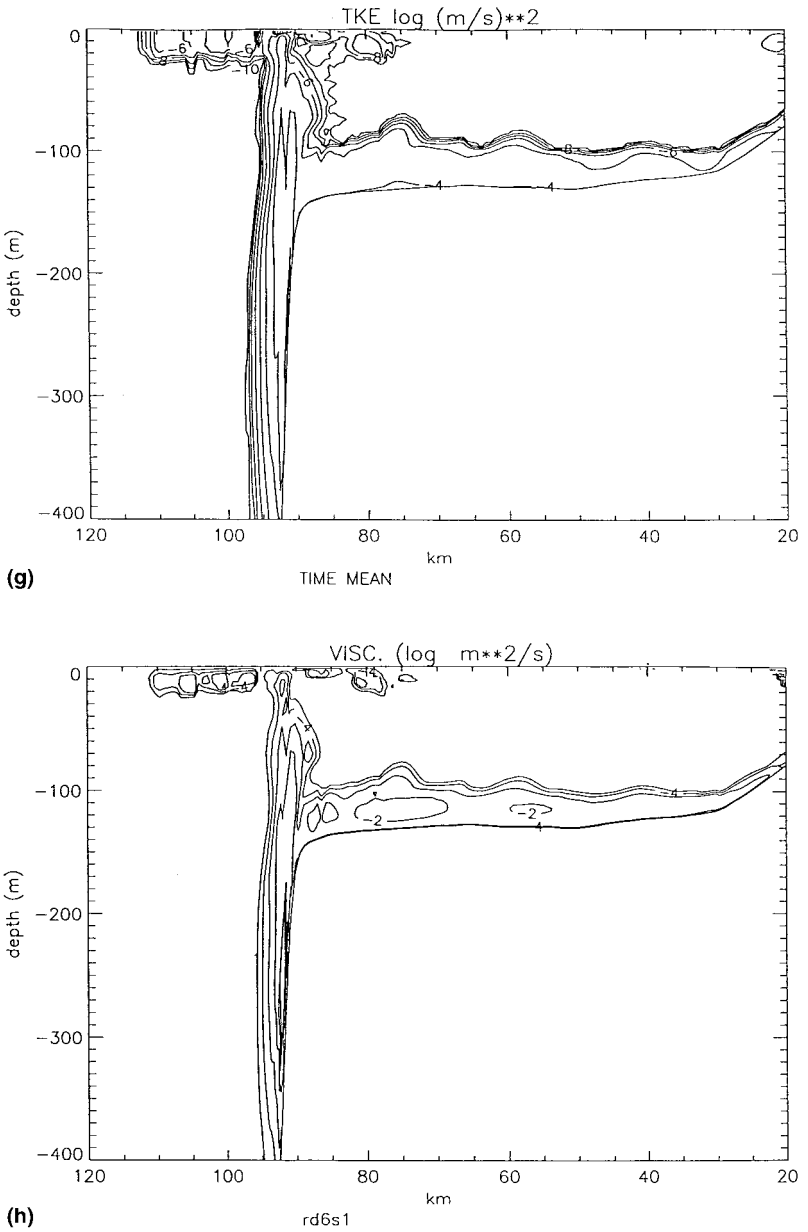

Figure 13 (*Continued*)

features were not present in calculation 9 due to the coarser topography used in this calculation.

Away from the shelf slope (about 170 km offshore) at a depth of 1200 m, there is a region of maximum current amplitudes (currents exceeding 8 cm s^{-1}). The location of the maximum is similar to that found previously although its intensity is larger (compare Figures 13(a) and 11(a)). Other differences are evident in the surface currents which show a number of regions of intensified current at offshore positions. The location of these positions is significantly

different from those found previously (compare Figures 13(a) and 11(a)) suggesting differences in the ray paths followed by the internal tide due to differences in shelf topography [2,5,36].

Contours of internal displacement (Figure 13(b)) show a region of rapidly changing internal displacement at the top of the shelf break with displacements significantly larger than those found previously (Figure 11(b)). Displacements along the shelf slope appear larger than previously with an area at a depth of 500 m situated about 98 km offshore where the internal displacement exceeds 24 m, and a region at about 108 km offshore where the internal displacement exceeds 20 m.

Since the model contains the non-linear terms responsible for generating the higher harmonics of the tide, it is instructive to examine the spatial distributions of the amplitude of the M_4 current and the internal displacement at this frequency. Comparing Figure 13(c) and (d) with those obtained previously (Figure 11(c) and (d)) it is evident that the M_4 tidal current is significantly larger in the near-bed region than that found previously. Similarly, the internal displacement at the top of the shelf break is larger than that found previously (Figure 11(d)) with large (of the order of 8 m) internal displacements occurring up to 108 km from the shore. Similarly, for the M_6 component of the tide, it is evident that the u current amplitude and internal displacement is a maximum in the region of the shelf slope (Figure 13(e) and (f)) and that this maximum is significantly larger than that found previously (Figure 11(e) and (f)). Contours of turbulence energy and viscosity (Figure 13(g) and (h)), show enhanced mixing at the top of the shelf slope compared with the calculation using smoothed topography (compare Figures 13(g) and (h) and 11(g) and (h)).

To understand the reasons for the enhanced vertical displacement at the top of the shelf, it is instructive to compare contours of σ_t computed previously with smoothed topography (calculation 9) (Figure 14) with those determined using the accurate topography (Figure 15) at the same moments in time over a tidal period after the model has been run for 30 periods.

Comparing σ_t contours at $t = \frac{1}{16}T$ (Figures 14 and 15) it is evident that the $\sigma_t = 28.10$ contour downwells more in the accurate topography calculation than that with coarser topography due to the steeper shelf slope. Also, above the shelf slope the magnitude of the shorter waves formed by the non-linear processes [6,34,38] is significantly larger in the calculation with accurate topography (calculation 11) than those found previously (calculation 9). Density contours at depth (of order 800 m) in both calculations show an upwelling along the shelf slope of the $\sigma_t = 28.45$ surface although away from the shelf slope the spatial variability of this contour is different due to differences in propagation of the internal tide arising from the differences in shelf slope.

At a later moment in the tidal cycle, namely $t = \frac{8}{16}T$ upwelling occurs in the region near the top of the shelf slope with the $\sigma_t = 28.10$ density surface at the shelf break moving from a depth of about 400m (Figure 15(i) $t = \frac{1}{16}T$) to about 270 m (Figure 15(ii) $t = \frac{8}{16}T$) an internal displacement of 130 m along the shelf slope although at distances a few km away from the slope the internal displacement is much less. In the case of the poorer resolution topography (Figure 14(ii)) upwelling at the top of the shelf break still occurs although the $\sigma_t = 28.10$ surface only moves from 240 m ($t = \frac{1}{16}T$) to 200 m, ($t = \frac{8}{16}T$) although the upwelling of the $\sigma_t = 28.15$ surface is much larger from 375 m to 275 m.

In the case of the higher resolution topography, upwelling of the density surfaces, which occurs in the region above the shelf slope (Figure 15(ii)), changes the horizontal spatial variability of the $\sigma_t = 28.5$ surface, although a sharp horizontal density gradient is still evident. The solution with lower resolution topography (Figure 14(ii)) also shows an upwelling of the density surfaces above the shelf slope again with significant horizontal spatial variability of the density surfaces although this variability is less than that found with the high resolution topography (compare Figures 15(ii) and 14(ii)).

Density surfaces at depth ($h = 800$ m) in both cases show a change from upwelling to downwelling against the shelf slope. However, the magnitude and location of this is different due to local differences in the gradient of the slope.

This comparison of internal tide generation using the same horizontal grid resolution but with water depths based on low resolution topography read from a chart (calculation 9) and

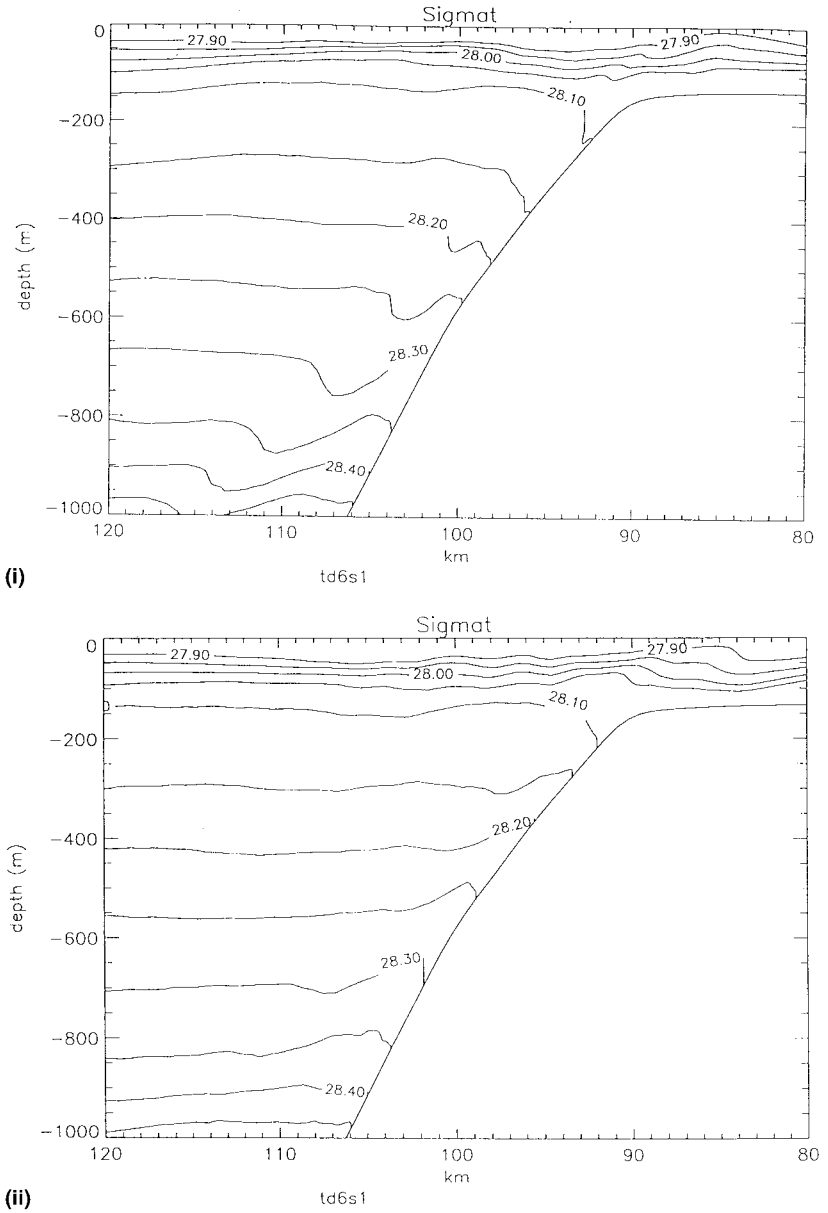

Figure 14. Contours (at the top of the shelf slope) of σ_t values after 30 tidal cycles at (i) $t = \frac{1}{16}T$ and (ii) $t = \frac{8}{16}T$ computed with the smoothed topography.

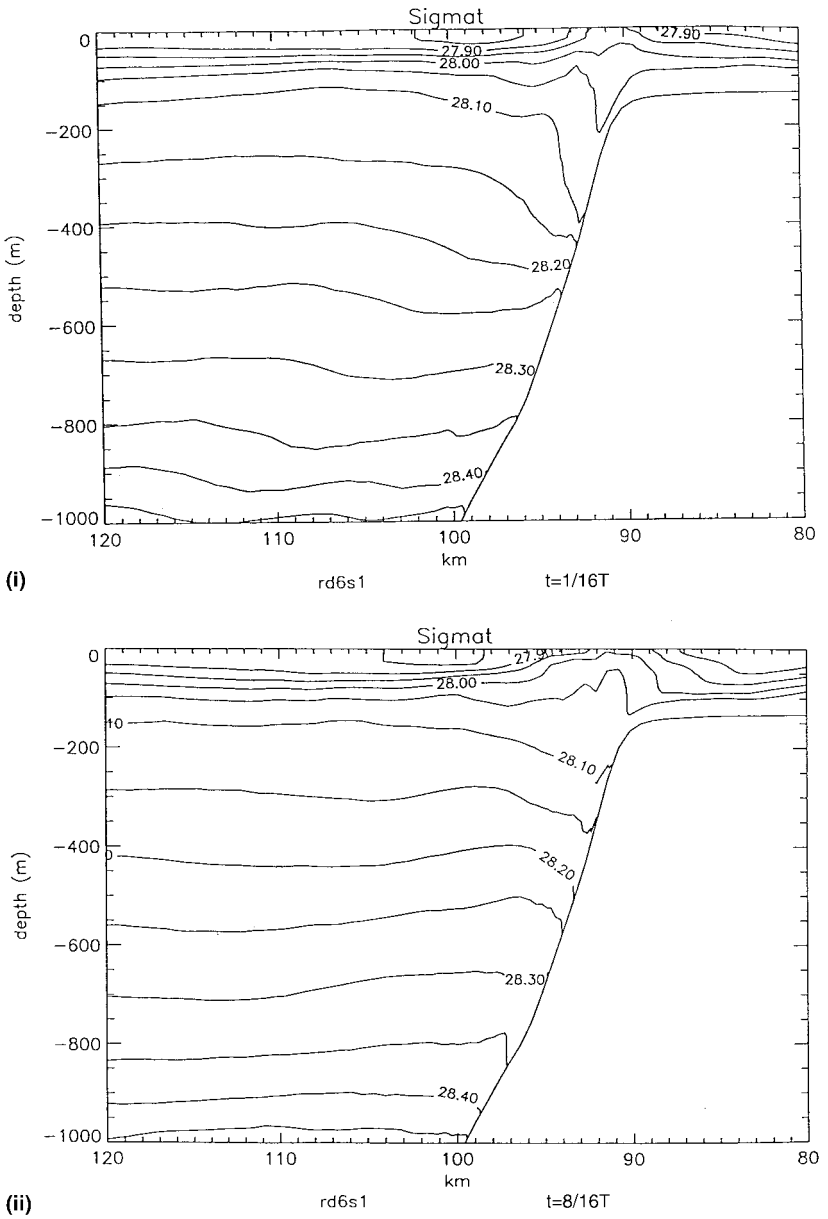

Figure 15. Contours of σ_t values after 30 tidal cycles at (i) $t = \frac{1}{16}T$ and (ii) $t = \frac{8}{16}T$ computed with the realistic topography.

high resolution topography from an accurate survey (calculation 11) clearly illustrates the importance of accurate topography in order to model the magnitude of internal tide displacement both over the shelf slope and offshelf.

5. CONCLUDING REMARKS

In this paper the major steps in developing a three-dimensional baroclinic model with a turbulence energy submodel, which is suitable for computing the internal tides in shelf edge regions have been briefly outlined. The model has been applied in cross-shelf form to examine the influence of seamounts, shelf slope, the non-linear terms and stratification upon the internal tide generation in the region off the west coast of Scotland, an area of a future intensive measurement programme. Although in cross-shelf form the model cannot take account of along-shelf variations in topography, or along-shelf changes in the tide, it does include the along-shelf velocity and rotational effects, and hence is adequate for the study considered here. The application of a cross-shelf model is particularly appropriate in the region considered here, where the major contribution to the on shelf tide is normal to the shelf edge. Cross-shelf models have been successfully used in such situations to simulate the internal tide [6,8,34,35,39,43].

A comparison of internal tidal current amplitudes and displacements with linear and non-linear models (i.e. the exclusion or inclusion of horizontal advection of momentum terms) (calculations 1 and 2) shows significant differences, with the non-linear model showing greater spatial variability and the generation of short internal waves above the top of the shelf slope. This suggests that calculations with linear models may omit important physical processes and that future calculations with three-dimensional models will need to include the non-linear terms.

Calculations of the internal tide at 56.5°N, a cross-section that has a seamount adjacent to the shelf slope, show that the seamount has an influence upon the internal tide, with a local internal tide being generated on the western and eastern sides of the seamount besides along the shelf slope. The combination of these internal tides can increase surface internal tidal currents and the associated mixing. The calculations (calculations 2 and 3) involving the shelf slope with and without the seamount, and calculations with the seamount in isolation (calculation 6), show that in such regions, the internal tide cannot be regarded as being produced entirely on the shelf slope. Consequently, an accurate description of the topography and density field in the region of the seamount is also required.

The calculations performed with a slightly modified density profile (calculations 4 and 5) clearly show that the internal tide is influenced by changes in the density field, suggesting that an accurate survey of the density distribution is essential. As shown in calculations 7 and 8, significant changes in the density field (i.e. changes between winter and summer) produce major changes in the internal tide both in a linear model (calculation 7) or when the non-linear terms are retained (calculation 8). In the summer time significant spatial variability in the currents, internal displacements and mixing is found in the near-surface layers, suggesting that observations are concentrated in this layer at this time of year. The calculations with summer stratification using both linear (calculation 7) and non-linear (calculation 8) models confirm the conclusions based upon winter stratification, namely that these terms need to be retained in all calculations no matter which seasonal density distribution is used.

Calculations 9 and 10 using the cross-section topography at 56°N with a smooth shelf slope, but assuming a well-mixed bottom boundary layer produced possibly by cold dense water cascading down the shelf slope, or a similar process, are used to investigate the influence of this bed layer. Comparisons of internal tide current magnitude and displacements with and without this well-mixed bed layer, show that with the bed layer, the internal tidal signal generated at the shelf edge can be reflected at the density interface and propagate much further offshelf. This offshelf propagation produces significantly stronger surface currents at greater distances

from the shelf edge than when the bottom mixed layer is absent. This calculation clearly illustrates the importance of collecting a detailed density distribution both in the region of internal tidal production, but also beyond the shelf slope in the near-bed region where internal tide reflection might occur.

The final series of calculations using, in essence, smoothed topography (calculation 9) compared with high resolution topography from a recent survey (calculation 11), illustrates the importance of an accurate topographic data set in computing internal tides. The high resolution topographic data set more accurately represents the shelf slope, and shows a number of regions of significant local change in the gradient of the shelf slope. Calculations reveal that local internal tides are generated in the region of these features that can lead to local intensive currents and mixing. This suggests that there is significantly greater spatial variability in nature than that found in previous models of the internal tide, which were based on smoothed topography. Also, an intensive observational data set will be required to examine this variability and to make rigorous model comparisons with data possible.

The calculations presented here illustrate the complexity of the internal tide generation off the west coast of Scotland and the need for a comprehensive observational data set including turbulence measurements [40–42] to validate the turbulence energy closure schemes. Future investigations will be concerned with the three-dimensional nature of the internal tide in this region.

ACKNOWLEDGMENTS

The authors are indebted to Mr R.A. Smith for help in preparing the figures and Mrs L. Ravera for typing the text.

REFERENCES

1. P.G. Baines, 'On internal tide generation models', *Deep-Sea Res.*, **29**, 307–338 (1982).
2. P.D. Craig, 'Solutions for internal tidal generation over coastal topography', *J. Marine Res.*, **45**, 83–105 (1987).
3. W.-S. Chuang and D.-P. Wang, 'Effects of density front on the generation and propagation of internal tides', *J. Phys. Oceanogr.*, **11**, 1357–1374 (1981).
4. T.J. Sherwin, 'Evidence of a deep internal tide in the Faeroe–Shetland Channel', in B.B. Parker (ed.), *Tidal Hydrodynamics*, Wiley, New York, 1991, pp. 469–488.
5. T.J. Sherwin and N.K. Taylor, 'The application of a finite difference model of internal tide generation to the NW European Shelf', *Dt. Hydrogr. Z.*, **42**, 151–167 (1989).
6. K.G. Lamb, 'Numerical experiments of internal wave generation by strong tidal flow across a finite amplitude bank edge', *J. Geophys. Res.*, **99**, 843–864 (1994).
7. A.L. New and R.D. Pingree, 'Evidence for internal tidal mixing near the shelf break in the Bay of Biscay', *Deep Sea Res.*, **37**, 1783–1803 (1990).
8. A.L. New, 'Internal tidal mixing in the Bay of Biscay', *Deep Sea Res.*, **35**, 691–709 (1988).
9. J. Xing and A.M. Davies, 'Processes influencing the internal tide, its higher harmonics and tidally induced mixing on the Malin–Hebrides Shelf', *Prog. Oceanogr.*, **38**, 155–204 (1997).
10. J. Xing and A.M. Davies, 'Formulation of a three-dimensional shelf edge model and its application to internal tide generation', *Cont. Shelf Res.*, **18**, 405–440 (1998).
11. J. Xing and A.M. Davies, 'Application of a range of turbulence energy models to the computation of the internal tide', *Int. J. Numer. Methods Fluids*, **26**, 1055–1084 (1998).
12. D.J. Ellett, A. Edwards and R. Bowers, 'The hydrography of the Rockall Channel—an overview', in *The Oceanography of the Rockall Channel: Proceedings of the Royal Society of Edinburgh*, 88B, 1986, pp. 61–81.
13. B.S. McCartney and J.M. Huthnance, Cruise Report RRS Charles Darwin, 91A 2–22 March, 91B 22 March–2 April 1995, LOIS Shelf Edge Study, Proudman Oceanographic Laboratory, *Cruise Report No. 20*, 1995.
14. J. Xing and A.M. Davies, 'Application of turbulence models to the computation of tidal currents and mixing intensities in shelf edge regions', *J. Phys. Oceanogr.*, **26**, 417–447 (1996).
15. J. Xing and A.M. Davies, 'Internal lee waves and turbulence mixing over an isolated seamount: results from a turbulence energy model', *Int. J. Numer. Methods Fluids*, **23**, 1–30 (1996).

16. A.D. Heathershaw, J. Small and C.E. Stretch, 'Frictional formulations in numerical ocean models and their effect on simulated acoustic fields', *J. Phys. Oceanogr.*, **24**, 274–297 (1994).
17. A.M. Davies and J. Xing, 'An intercomparison and validation of a range of turbulence energy schemes used in three dimensional tidal models', in D.R. Lynch and A.M. Davies (eds.), *Qualitative Skill Assessment for Coastal Ocean Models*, AGU Coastal and Estuarine Series, 1995, pp. 71–96.
18. J. Xing and A.M. Davies, 'The influence of mixing length formulation and stratification upon tidal currents in shallow seas', *Estuarine Coast. Shelf Sci.*, **42**, 417–456 (1996).
19. J. Xing and A.M. Davies, 'Application of a range of turbulence energy models to the determination of M_4 tidal current profiles', *Cont. Shelf Res.*, **16**, 517–547 (1996).
20. I.D. James, 'Advection schemes for shelf sea models', *J. Marine Syst.*, **8**, 237–254 (1996).
21. A.M. Davies and J.E. Jones, 'Application of a three-dimensional turbulence energy model to the determination of tidal currents on the northwest European shelf', *J. Geophys. Res.*, **95**, 18143–18162 (1990).
22. A.M. Davies and J.E. Jones, 'On the numerical solution of the turbulence energy equations for wave and tidal flows', *Int. J. Numer. Methods Fluids*, **12**, 17–41 (1991).
23. H. Baumert and G. Radach, 'Hysteresis of turbulent kinetic energy in non-rotational tidal flows: a model study', *J. Geophys. Res.*, **97**, 3669–3677 (1992).
24. B. Johns and T. Oguz, 'Turbulent energy closure schemes', in N.S. Heaps (ed.), *Three-Dimensional Coastal Ocean Models*, American Geophysical Union, Washington, DC, 1987, pp. 17–40.
25. P.J. Luyten, E.L. Deleersnijder, K.G. Ruddick and J. Ozer, 'Presentation of a family of turbulence closure models for stratified shallow water flows and preliminary application to the Rhine outflow region', *Cont. Shelf Res.*, **16**, 101–130 (1996).
26. P.J. Luyten, 'An analytical and numerical study of surface and bottom boundary layers with variable forcing and application to the North Sea', *J. Marine Syst.*, **8**, 171–190 (1996).
27. C.E. Naimie, J.W. Loder and D.R. Lynch, 'Seasonal variation of the three-dimensional residual circulation on Georges Bank', *J. Geophys. Res.*, **99**, 15967–15989 (1994).
28. A.F. Blumberg and G.L. Mellor, 'A description of a three-dimensional coastal ocean circulation model', in N.S. Heaps (ed.), *Three-Dimensional Coastal Ocean Models*, (Coastal and Estuarine Sciences, No. 4), American Geophysical Union, Washington, DC, 1987, pp. 1–16.
29. L.-Y. Oey and P. Chen, 'A nested-grid ocean model: with application for the simulation of meanders and eddies in the Norwegian coastal current', *J. Geophys. Res.*, **97**, 20063–20086 (1992).
30. B. Galperin, L.H. Kantha, S. Hassid and A. Rosati, 'A quasi-equilibrium turbulent energy model for geophysical flows', *J. Atmos. Sci.*, **45**, 55–62 (1988).
31. B. Galperin, A. Rosati, L.H. Kantha and G.L. Mellor, 'Modelling rotating stratified turbulent flows with application to oceanic mixed layers', *J. Geophys. Res.*, **94**, 901–916 (1989).
32. E.A. Martinsen and H. Engedahl, 'Implementation and testing of a lateral boundary scheme as an open boundary condition in a barotropic ocean model', *Coast. Eng.*, **11**, 603–627 (1987).
33. D.T. Pugh, *Tides, Surges and Mean Sea Level*, Wiley, New York, 1987.
34. P.E. Holloway, 'On the semi-diurnal internal tide at a shelf-break region on the Australian north-west shelf', *J. Phys. Oceanogr.*, **14**, 1778–1790 (1984).
35. T.J. Sherwin, 'Analysis of an internal tide observed on the Malin Shelf, north of Ireland', *J. Phys. Oceanogr.*, **18**, 1035–1050 (1988).
36. T.J. Sherwin and N.K. Taylor, 'Numerical investigations of linear internal tide generation in the Rockall Trough', *Deep Sea Res.*, **37**, 1595–1618 (1990).
37. P.E. Holloway, 'A numerical model of internal tides with application to the Australian North West Shelf', *J. Phys. Oceanogr.*, **26**, 21–37 (1996).
38. P.E. Holloway, 'On the dissipation of internal tides', in B.B. Parker (ed.), *Tidal Hydrodynamics*, Wiley, New York, 1991, pp. 449–468.
39. A.D. Heathershaw, A.L. New and P.D. Edwards, 'Internal tides and sediment transport at the shelf break in the Celtic Sea', *Cont. Shelf Res.*, **7**, 485–517 (1987).
40. A.E. Gargett, 'Observing turbulence with a modified acoustic doppler current profiler', *J. Atmos. Ocean. Technol.*, **11**, 1592–1610 (1994).
41. H. Sandstrom and N.S. Oakey, 'Dissipation in internal tides and solitary waves', *J. Phys. Oceanogr.*, **25**, 604–614 (1995).
42. J.H. Simpson, W. Crawford, T.P. Rippeth, A.R. Campbell and J.V.S. Cheok, 'The vertical structure of turbulent dissipation in shelf seas', *J. Phys. Oceanogr.*, **26**, 1579–1590 (1996).
43. R. Maze, 'Generation and propagation of non-linear internal waves induced by the tide over a continental slope', *Cont. Shelf Res.*, **7**, 1079–1104 (1987).

